THESIS FOR THE DEGREE OF DOCTOR OF PHILOSOPHY
IN NATURAL SCIENCE, SPECIALISING IN CHEMISTRY

MECHANISTIC INSIGHTS INTO TRANSITION METAL OXIDE CATALYZED WATER OXIDATION

MICHAEL BUSCH

UNIVERSITY OF GOTHENBURG

Department of Chemistry and Molecular Biology
University of Gothenburg
Gothenburg, Sweden
June 2012

Mechanistic Insights into Transition Metal Oxide Catalyzed Water Oxidation

Department of Chemistry and Molecular Biology
University of Gothenburg
SE-412 96 Gothenburg
Sweden
E-mail: michael.busch@chem.gu.se

ISBN: 978-91-628-8480-2
Online available at: http://hdl.handle.net/2077/29099

Printed by Chalmers Reproservice

"Forty-two," said Deep Thought, with infinite majesty and calm.

(*The Hitchhiker's Guide to the Galaxy*, Douglas Adams)

ABSTRACT

A binuclear mechanism was proposed and evaluated by means of Density Functional Theory calculations. The central reaction steps were found to be the oxidation of the transition metal TM-OH moieties to TM=O and the subsequent intramolecular O-O bond formation between two TM=O groups. These step were employed as descriptors for the performance of a set of 3d transition metal oxides studied in a $MgO_x(OH)_y$ test rig embedding. Two classes of oxygen evolution reaction (OER) catalysts were found to emerge at the TyrOH/TyrO$^\bullet$ reference potential. The first class, referred to as [+/-], which contains Mn(III-V), Co(II-IV) and Ni(II-IV), shows an endothermic oxidation step combined with exothermic O-O bond formation. The members of this class were argued to be active towards the (OER), i.e. the oxy moieties desorb spontaneously as O_2 at the expense of high overpotentials. The second class, called [-/+], comprising V(III-V), Cr(III-V) and Fe(II-IV), was found to show opposite behavior. Thus, poor performance is expected due to a highly unfavorable O-O bond formation step. Improved performance was predicted by mixing [+/-] with [-/+] transition metal oxides. Intermediate behavior, meaning oxidation of the TM-OH moiety to TM=O at the TyrOH/TyrO$^\bullet$ potential combined with a thermoneutral O-O bond formation, is found for Ir(III-V) and Mn(II-IV). While the former displays high activity towards the water oxidation reaction the latter is argued to be inactive due to unfavorable kinetics. The idea of mixing transition metal oxides was generalized for mixed oxidation state systems and evaluated for a Mn(II-IV) Mn(III-V) system. Improved performance was found suggesting, that this reaction path is relevant for the (OER). The generality of the mechanism was shown by direct comparison with experimental findings on iridium oxide and RuO_2.

LIST OF PUBLICATIONS

This thesis is based on the following publications. Whithin the text they will be referred to by their roman number.

I Switching on the Electrocatalytic Ethene Epoxidation on Nanocrystalline RuO_2
J. S. Jirkovský, M. Busch, E. Ahlberg, I. Panas and P. Krtil, *J. Am. Chem. Soc.*, **133** (2011), p.5882-5892

II Activation Energies in Computational Chemistry - A Case Study
M. Busch, E. Ahlberg and I. Panas, in *Rate Constant Calculation of Thermal Reactions: Methods and Applications*, p.93-111 John Wiley & Sons, 2012

III Electrocatalytic oxygen evolution from water on a Mn(III-V) dimer model catalyst - A DFT perspective
M. Busch, E. Ahlberg and I. Panas, *Phys. Chem. Chem. Phys.*, **13** (2011), p.15069-15076

IV Hydroxide oxidation and peroxide formation at embedded binuclear transition metal sites; TM = Cr, Mn, Fe, Co
M. Busch, E. Ahlberg and I. Panas, *Phys. Chem. Chem. Phys.*, **13** (2011), p.15062-15068

V Validation of binuclear descriptor for Mixed Transition Metal Oxide supported Electrocatalytic Water Oxidation
M. Busch, E. Ahlberg and I. Panas, submitted to *Catal. Today*

VI Water Oxidation on MnO_x and IrO_x - Why Similar Performance?
M. Busch, E. Ahlberg and I. Panas, submitted to *Angew. Chem.*

VII Electrodeposited Hydrous Iridium Oxide Films: Experiments and DFT Calculations
P. Steegstra, M. Busch, I. Panas, E. Ahlberg, in Manuscript

STATEMENT OF CONTRIBUTIONS

I Contributed to the mechanistic understanding.

II Performed all calculations, interpreted the results, lead author of the manuscript.

III Performed all calculations, interpreted the results, lead author of the manuscript.

IV Performed all calculations, interpreted the results, lead author of the manuscript.

V Performed all calculations, interpreted the results, lead author of the manuscript.

VI Performed all calculations, interpreted the results, lead author of the manuscript.

VII Performed all calculations, contributed to the interpretation of the results and the writing of the paper.

CONTENTS

LIST OF ABBREVIATIONS

acac	acetylacetonate
CV	cyclic voltammogram
DFT	Density Functional Theory
DSA	Dimensionally Stable Anode
GGA	generalized gradient approximation
GTO	Gaussian-type orbital
HER	hydrogen evolution reaction
HOMO	highest occupied molecular orbital
IR	infra red
KS	Kohn-Sham
LSDA	local spin-density approximation
LST	linear synchronous transit
LUMO	lowest unoccupied molecular orbital
NEB	nudged elastic band
NHE	normal hydrogen electrode
OER	oxygen evolution reaction
pdial	propane dialdehyde
PS II	Photosystem II
QST	quadratic synchronous transit

SCF	Self Consistant Field
SIE	self-interaction error
STO	Slater-type orbital
TM	transition metal
TyrO•	tyrosyl radical
TyrOH	tyrosine
xc	exchange-correlation

1 INTRODUCTION

The splitting of water into hydrogen reducing equivalents and oxygen plays a central role in the quest for new energy carriers that can replace fossil fuels [1–3]. In electrochemical water splitting the hydrogen evolution reaction (HER) is catalyzed efficiently by many noble metals such as platinum[4–7] or alternatively in alkaline solution by non noble metals such as cobalt[8] or nickel[9]. The corresponding anode reaction for the production of the (H^+/e^-) reducing equivalents are unfortunately more complicated.

These complications and the importance of the oxygen evolution reaction (OER) is resembled by the constant interest in this reaction over the last decades[3, 10, 11]. With the rise of Dimensionally Stable Anodes (DSAs)[12–14] approximately 50 years ago efficient electrocatalysts to facilitate electrocatalytic water oxidation in industry exist. These anodes are the state of the art in industrial electrocatalysis. The active catalyst in DSAs consists of a mixture of RuO_2, TiO_2 and in minor amounts also other oxides such as IrO_2[15] painted on a titanium electrode[12–14, 16]. Even though such electrocatalysts exhibit long term stability up to 10 years[14] even under harsh conditions[17], they are based on rare and expensive materials, which make it desirable to replace them by more abundant and thus cheaper oxides with a similar or better performance. Candidate materials are transition metal oxides such as manganese[18, 19] and cobalt oxides[20–23].

Nature in contrast employs a rather different approach to catalyze the OER. The catalyst employed in the biological OER, Photosystem II (PS II), which is embedded into a large protein matrix is based on abundant manganese. The active catalytic center of PS II is known to consist of a Mn_4O_4 tetramer[24–27]. This system is able oxidize the OER at a low overpotential with a high efficiency[28–30]. The price tag for employing a molecular catalyst based on abundant manganese oxide is the low stability[31, 32].

The efficiency of green plants to perform the photosynthesis has provided great inspiration to the field of artificial photosynthesis. Similarly to biological photosynthesis it is attempted to convert sunlight directly into chemical energy.

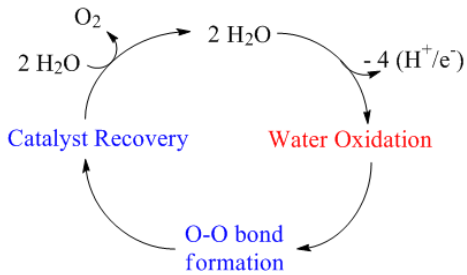

Figure 1: The general steps in any OER mechanism are depicted. Electrochemical steps are colored red and chemical steps blue.

A typical system for artificial photosynthesis consists of an antenna used to collect sunlight, the catalytic sites where the actual water splitting happens and a reaction center that generates an electron-hole separated state required to drive the chemical reactions at the catalytic sites[33]. The systems discussed as possible biomimetic water oxidation catalysts are, inspired by the OER in PS II, transition metal complexes[3, 34–37] based on ruthenium[38–40], manganese[41–44] or iridium[45, 46] with up to four transition metal cores. The choice of a molecular system has several advantages. One is the possibility to directly influence the electronic structure of the transition metal core and thus, the redox chemistry of the complex, by the choosing the appropriate ligand. Furthermore molecular species exhibit a comparably higher flexibility, which can support the O-O bond formation in a binuclear OER mechanism. Unfortunately molecular OER catalysts suffer from deactivation[41, 42]. This renders their use in industrial applications, where long term stability is required, problematic.

Despite the large differences in catalyst design any candidate OER catalyst must be able to catalyze several key steps. An overview over the key steps in any OER mechanism is shown in Figure 1. Considering the starting point of any water oxidation reaction to be two water molecules it is necessary to remove in total 4 (H^+/e^-) reducing equivalents in a series of consecutive oxidation steps at a minimum overpotential. Having oxidized, depending on the detailed OER mechanism, one or two H_2O molecules to surface oxo species, it is necessary to recover the catalyst. Assuming oxygen evolution this is done by an O-O bond formation followed by the release of $^3O_2$. In the case of a binuclear mechanism the former reaction step is purely chemical, while it is an electrochemical step

in the case of a mononuclear mechanism[47, 48]. The main challenge in the design of active OER catalysts is the necessity to remove the (H^+/e^-) couples at an as low overpotential as possible while the resulting intermediate needs to be sufficiently reactive to facilitate the O-O bond formation. This necessary compromise can be expressed in a volcano plot, which is constructed based on Sabatier's principle. In the volcano plot the optimal catalysts can be found on top of the curve.

The role of theory in this quest for catalysts, that show optimal behavior for both critical reaction steps, can be manifold. The most fundamental approach is to generate a mechanistic understanding of the OER. Based on this understanding, design criteria for new enhanced catalysts can be identified and possible descriptors can be developed. With the knowledge of design criteria and possible descriptors, theory can become a tool to scan the reactivity of a large number of candidate catalysts in a cheap and efficient manner. A possible way to represent such data is for example the representation in a volcano plot[4, 49]. This representation has been employed successfully to many problems[6, 50].

In the present work a combined approach of a fundamental mechanism study followed by the scanning of a set of 3d transition metal oxide candidate systems is performed. The mechanistic study was carried out, employing a molecular manganese dimer model system based on existing biomimetic catalysts[38, 39, 41–44]. The insights gained from this study were used to extract the critical steps in water oxidation. These were found to comprise the oxidation of transition metal (TM) hydroxo moieties to form TM oxo groups and the subsequent O-O bond formation. In the following series of studies these two reaction steps were employed as descriptors for the reactivity of 3d transition metal oxides. All studied 3d transition metals were found to either exhibit a large overpotential in combination with a strongly exothermic O-O bond formation step or to form the oxo intermediates at a too low potential resulting in a strongly endothermic O-O bond formation. Based on the discovery of these two reactivity classes the existence of OER catalysts with cancellation of endothermicity and exothermicity thus, showing near ideal behavior, was predicted for a mixed oxide containing one transition metal oxide from each class. This concept was evaluated for a set of mixed 3d transition metal oxides and generalized for mixed oxidation state systems, where a similar behavior was found.

2 THEORETICAL BACKGROUND

2.1 THE SCHRÖDINGER EQUATION

The fundamental equation one tries to evaluate by means of any quantum chemical method is the time independent non relativistic Schrödinger equation. This equation was proposed the first time, inspired by the Hamilton-Jacobi formalism derived for classical mechanics and the wave description of electrons introduced by de Broglie, by Erwin Schrödinger in 1926[51]. The similarities between the Hamilton-Jacobi formalism and the Schrödinger equation can be appreciated considering that the former is given by

$$H(q, \underbrace{\frac{\partial S}{\partial q}}_{p}) = \underbrace{\frac{\partial S}{\partial t}}_{E} \tag{1}$$

where **q** is the space coordinate, S is an action and **p** is the momentum and time-dependent Schrödinger equation reads

$$\hat{H}\Psi = i\hbar\frac{\partial \Psi}{\partial t} \tag{2}$$

A major difference between the Hamilton-Jakobi equations for classical mechanics and the Schrödinger equation lies in the fact that the classical systems, described by the Hamilton-Jacobi formalism, are fully determined, assuming the complete Hamilton function is known. This is no longer the case for quantum mechanical systems.

In the case of quantum chemical calculations, time independent situations are considered in most cases. A time independent situation is arrived at by splitting up the wave function Ψ into:

$$\Psi(\mathbf{r}, t) = \Psi(\mathbf{r}) \exp\left(-i\frac{Et}{\hbar}\right) \tag{3}$$

where the time dependent Schrödinger equation goes over into the time independent formulation for t=0.

$$\hat{H}\Psi = E\Psi \tag{4}$$

In this differential equation E corresponds to the energy eigenvalue of the Schrödinger equation and Ψ is the wave function. The interpretation of the meaning of the wave function is unfortunately not straightforward. While Ψ itself has no physical interpretation besides its mathematical meaning as an eigenfunction, the square of the wave function $|\Psi|^2$ is commonly interpreted as probability density[52, 53]. $\hat{H}$ is the Hamiltonian, which is an energy operator that contains all relevant energy operators for the system at hand. In the case of an atomic or molecular situation, which is equal to a situation of a number of electrons in the field of nuclei, this operator contains the repulsive interactions between the nuclei $V_{nucl-nucl}$ and electrons V_{el-el}, the attractive interactions between nuclei and electrons $V_{el-nucl}$ as well as the kinetic energy operators of the nuclei T_{nucl} and electrons T_{el}.

$$\hat{H} = T_{el} + T_{nucl} + V_{nucl-nucl} + V_{el-el} + V_{nucl-el} \tag{5}$$

Again by applying the correspondence principle between classical and quantum mechanics the kinetic energy operator can be defined as

$$\sum_i \frac{p_i^2}{2m_i} \tag{6}$$

where m is the mass of the particle and the momentum $\mathbf{p}$ is defined as

$$p = -i\hbar\nabla \tag{7}$$

In principle it would now be possible with the knowledge of the Schrödinger equation and the appropriate Hamiltonian for atomic and molecular systems to solve any quantum chemical problem exactly. In reality an exact analytical solution is only possible for a few systems such as the hydrogen atom[51, 54] or H_2^+[54]. All other systems require at least two approximations. One is the Born-Oppenheimer approximation[53, 55–57]. The central idea of this approximation is to separate the electronic and nucleus parts of the Schrödinger equation. This is possible since the mass of electrons is much smaller compared to the nuclei, typically by an order of magnitude of 10^4 to 10^5. Thus, the nuclei can be expected

to move much slower compared to the electrons, resulting in electrons moving in the field of approximately static nuclei. This allows to separate the electronic part of the Schrödinger equation from the nucleus part as the electronic part of the wave function becomes only parametrically dependent on nuclear coordinates.

$$\Psi_{tot} = \Psi_{el}\Psi_{nucl} \tag{8}$$

By varying the external potential defined by the coordinates of the nuclei the Born-Oppenheimer potential energy surface is obtained.

$$\epsilon_{tot}(\mathbf{R}) = \epsilon_{el}(\mathbf{R}) + V_{nucl-nucl}(\mathbf{R}) \tag{9}$$

While this approximation serves well in most cases transitions between different potential energy surfaces can no longer be described within the framework of the Born-Oppenheimer approximation.

2.2 THE HARTREE–FOCK EQUATION

While the Born-Oppenheimer reduces the complexity of the Hamiltonian it does not explain why it is only possible to solve the Schrödinger equation analytically for 1 electron systems. The reason for this is the complexity of the manybody wave function, which can not be handled due to the complications resulting from the electron-electron interactions. For multi-electron systems this problem is attacked by decoupling the electrons and reducing the problem to 1 electron equations, which can be solved without problems[56]. The price tag of this procedure is, that the resulting 1-electron wave function is no longer equal to the true manybody wave function.

One of the first practical implementations to solve the electronic Schrödinger equation for multi-electron systems within the independent particle and Born-Oppenheimer approximations are the Hartree-Fock equations[56, 57]. This ansatz is the heart of all modern quantum chemical methods. It was developed by Hartree[58, 59] and later improved by Fock[60, 61] and Slater[62] independently by introducing the exchange term and the Slater determinant formulation of the wave function. In the Hartree-Fock ansatz the electronic part of the atomic Hamiltonian, described in Equation 5, is used to solve the electronic Schrödinger equation. Thus, the Hamiltonian consists of the kinetic energy of the electrons T_{el}, the electrostatic interactions between electrons and

nuclei, which define the external potential ($v_{ext}(\mathbf{r})$) the electrons are moving in, and the Hartree potential $v_{Hartree}(\mathbf{r})$, which describes the interactions between the electrons. In order to reduce the computational effort the exact position of the electrons are replaced by the effective potential of the surrounding electrons. However, it was soon realized that this ansatz is not sufficient since it does not account for the Pauli principle and contains the interaction of an electron with itself. These shortcomings were solved by introducing an exchange term and a Slater determinant ansatz for the wave function. The resulting Hartree-Fock equation is then

$$\left\{ \underbrace{-\frac{\hbar^2}{2m}\nabla^2}_{T_{el}} + \underbrace{-\sum_I \frac{Z_I e^2}{|\mathbf{r}-\mathbf{R_I}|}}_{v_{ext}(\mathbf{r})=v_{nucl-el}(\mathbf{r})} + \underbrace{\sum_j \int d^3\mathbf{r}' \frac{e^2}{|\mathbf{r}-\mathbf{r}'|}|\Psi_j(\mathbf{r}')|^2}_{v_{Hartree}(\mathbf{r})=v_{el-el}(\mathbf{r})} \right\} \Psi_i(\mathbf{r}) - \underbrace{\sum_j \int d^3\mathbf{r}' \frac{e^2}{|\mathbf{r}-\mathbf{r}'|}\Psi_j^*(\mathbf{r}')\Psi_i(\mathbf{r}')\Psi_j(\mathbf{r})\delta_{\sigma_i\sigma_j}}_{E_x} = \epsilon_i \Psi_i(\mathbf{r}) \tag{10}$$

While the kinetic energy and electrostatic contributions are describing a physical situation, the exchange energy part E_x is required to subtract the interactions of the electrons with itself and other electrons of the same spin in the same spatial region, which is introduced by the Hartree potential $v_{Hartree}$. Thus, E_x is equal to $v_{Hartree}$ when electron i is equal to electron j and zero for all other cases. Having solved all 1-electron Hartree-Fock equations the total energy of the system can finally be obtained from:

$$\epsilon_{tot} = \sum_i \epsilon_i - v_{Hartree} - E_x + v_{nucl-nucl} \tag{11}$$

The subtraction of the Hartree potential is necessary in order to avoid double counting.

Even though the Hamiltonian used to calculate the total energy is in principle exact for a non-relativistic system within the Born-Oppenheimer approximation, the energies obtained with the Hartree-Fock equation are generally poor compared to the exact total energy[63]. This deviation, which is generally negative,

i.e. the Hartree-Fock energy is always larger than the exact energy, is called correlation energy[56]. The correlation effects can be attributed to inaccuracies resulting from the erroneous description of the correlated electron movement, which results in a too weak repulsion of electrons in the effective potential used in Hartree-Fock (dynamic correlation). A second contribution to the correlation energy is the static correlation. Static correlation concerns the fact that only a single determinant is used to describe the wave function in the Hartree-Fock method. Although this approximation is valid in many cases it may not be sufficient for the ground state of all structures. The latter effect is especially problematic in systems were the ground state consists of several near-degenerate states as it can often be found in transition metal chemistry[64].

In *ab initio* quantum chemistry a rich set of tools was developed to deal with both dynamic and static correlation effects. These methods would in principle allow for very accurate results by systematic improvement of the basis set and methodology. A major drawback however results from the comparably high computational costs rendering these methods inapplicable for larger systems.

2.3 DENSITY FUNCTIONAL THEORY

A complementary ansatz to solve the electronic Schrödinger equation is Density Functional Theory (DFT). In pure DFT, which is based on the theorem by Hohenberg and Kohn[65], the electron density is used instead of the wave function. In the Hohenberg-Kohn theorem a connection between the external potential and the electron density is made by proofing that a unique external potential $v_{ext}(\mathbf{r})$ exists for any ground state electron density $n(\mathbf{r})$[65–67].

$$n(\mathbf{r}) \longrightarrow v_{ext}(\mathbf{r}) + const \tag{12}$$

This means in the case of an atomic or molecular system that, if the exact electron density $n(\mathbf{r})$ is known for the system at hand, the external potential $v_{ext}(\mathbf{r})$ containing all information about the electrostatic interactions between the electrons and nuclei is exactly defined. Together with the fact that the number of electrons is known via the relationship

$$N = \int n(\mathbf{r}) d^3\mathbf{r} \tag{13}$$

the Hamiltonian of the system would be known exactly. This would in principle allow for an exact solution of the electronic Schrödinger equation. However, this relationship is unfortunately only implicit[57], which renders the Hohenberg-Kohn theorem inapplicable for any practical problem in a direct manner.

Having this limitation of DFT in mind, a more practical formulation is required to solve computational chemistry problems. Such a formulation of DFT are the Kohn-Sham (KS) equations[68].

$$\left\{ -\frac{\hbar^2}{2m}\nabla^2 + \underbrace{v_{ext}(\mathbf{r}) + v_{Hartree}(\mathbf{r}) + v_{xc}(\mathbf{r})}_{v_{eff}(\mathbf{r})} \right\} \Psi_i(\mathbf{r}) = \epsilon_i \Psi_i(\mathbf{r}) \tag{14}$$

In the KS formulation of DFT, which is inspired by Hartree-Fock theory, the electron density $n(\mathbf{r})$ used in pure DFT is replaced by a wave function ansatz

$$n(\mathbf{r}) = \sum_{i=1}^{N} |\Psi_i(\mathbf{r})|^2 \tag{15}$$

and an additional term, the exchange-correlation functional $v_{xc}(\mathbf{r})$ is added, which contains the correlation effects and the non-classical part of the kinetic energy of the electrons.

When comparing the KS implementation of DFT as formulated in Equation 14 with the Hartree-Fock equations in Equation 10 many similarities can be found. The Hartree-Fock equations can indeed be obtained from KS-DFT by neglecting the exchange-correlation functional in KS-DFT and removing the exchange term in Hartree-Fock. Even though the eigenvalues and eigenfunctions obtained from the KS equations have little physical meaning[57, 67] they are successfully interpreted as the correct one-particle energies and are used to calculate the total energy of the system at hand via

$$\begin{aligned} E_{tot} = \sum_i \int |\phi_i(\mathbf{r})| \frac{\hbar^2}{2m}\nabla^2 d\mathbf{r} + \\ \sum_i \sum_j \int\int |\phi_i(\mathbf{r})|^2 \frac{e^2}{|\mathbf{r}-\mathbf{r}'|} |\phi_j(\mathbf{r}')|^2 d\mathbf{r} d\mathbf{r}' + \\ E_{xc}[\rho(\mathbf{r})] - \sum_i \int \sum_A \frac{Z_A e^2}{|\mathbf{r}-\mathbf{R_A}|} |\phi_i(\mathbf{r})|^2 d\mathbf{r} \end{aligned} \tag{16}$$

If the exact exchange-correlation functional is known, the total energies obtained with Equation 16 would be exact within the Born-Oppenheimer approximation for a non-relativistic system. In reality the exact form of E_{xc} is unfortunately unknown and can only be approximated, which introduces severe complications. In the following the term "DFT" will be used meaning the KS formulation of DFT if not explicitly mentioned otherwise.

2.4 THE EXCHANGE-CORRELATION FUNCTIONAL

Having learned that the exact functional E_{xc} is not known, a large number of approximated functionals were developed over the years. Any functional is constructed of an exchange and correlation part. The former contribution has a similar role compared to the Hartree-Fock exchange. However, additional to removing the interaction of an electron with itself, it contains some static correlation contributions[64, 69, 70]. In principle this contribution to the exchange-correlation (xc) functional is known exactly from Hartree-Fock theory. However, it is found that the usage of approximated exchange functionals gives better results due to a cancellation of errors with the non-exact correlation functional [64, 66]. The DFT correlation on the other hand takes care of the dynamic correlation effects. This part of the xc functional is not known exactly.

The simplest approximation for an xc functional is the local spin-density approximation (LSDA). Within the LSDA the electron density is approximated by a homogeneous electron gas. This means, that the electron density is assumed to be constant at every point. The functional for such a homogeneous electron gas is known with high accuracy[67, 68, 71]. Such an approximation of an electron gas is an acceptable approximation for strongly delocalized systems such as metals. For systems of this type, which are at least somewhat similar to an homogeneous electron gas, results within an error margin of 10%-20% for the energy and bond lengths within 1% can be expected for LSDA[66]. While this ansatz works astonishingly well for this type of systems, more localized electronic structures, as they can be found in molecules, are known to be problematic. Indeed, LSDA can be expected to fail completely due to the strong variations of the electron density over the whole compound[57, 67].

The inaccuracy of the LSDA functionals can be understood considering the fact, that they do not take the influence of a varying electron density into ac-

count. Thus, the next logic step in improving the xc-functionals is by considering the variation of electron density in the close proximity. This is done in the generalized gradient approximation (GGA) functionals. Here, the information about the surrounding is added by additionally considering the gradient of the electron density[57, 67, 72]. As a result of this improved treatment an accuracy was arrived at that made it possible to apply DFT to chemical problems. Typically GGA functionals are constructed in such a manner that they contain separated exchange and correlation parts that can be combined to a total xc functional. The construction of the approximate exchange functionals is in general mostly guided by the accuracy of the mathematical formulation with respect to the quality of the results rather than by the physics behind[67]. Typical exchange functionals used for GGA calculations are among others the exchange functional by Becke, B88[73], by Perdew, P86[74], or by Perdew, Burke and Enzerhof, PBE[75]. Often used GGA correlation functionals are the LYP functional derived by Lee, Yang and Parr[76] which is based on the model for the correlation energy of a helium atom derived by Colle and Salvetti[67, 77, 78], or the functional by Perdew Burke and Enzerhof (PBE)[75]. Despite the large variety of different GGA functionals the results obtained when employing different functionals are in most cases very similar[67].

While already the GGA exchange functionals typically contain a parameter that is fitted such that the functionals show optimal performance[67], additional improvement may be obtained by adding a certain amount of exact exchange taken from Hartree Fock. The functionals obtained by this ansatz are so called hybrid functionals. The amount of exact exchange, LSDA exchange and GGA exchange is varied by parameters. The numbers of parameters used is defined in the name of the functional, i.e. in B3LYP three parameters are employed, while PBE1PBE requires only one parameter. The typical form of such a functional is given for the B3LYP[79] functional employed in the present work:

$$E_{xc}^{B3LYP} = (1-a)E_X^{LSDA} + aE_X^{exact} + bE_X^{B88} + cE_C^{LYP} + (1-c)E_C^{LSDA} \qquad (17)$$

In the construction of the B3LYP functional the B88[73] GGA exchange together with some amount of LSDA exchange and correlation and the LYP[76] correlation functional is used. The amount of exact exchange in this functional is 20%. A formulation optimized to the low spin - high spin energy difference in iron complexes containing only 15% was suggested by Reiher et al.[80]. Generally functionals of this type show good performance for many applications[81, 82].

2.5 MAJOR FLAWS OF DFT

While the KS formulation of DFT is still exact, given the exact xc-functional would be known, this is no longer the case when employing the approximate functionals presented in Section 2.4. Here, two serious flaws are introduced into DFT, the self-interaction error (SIE)[67, 70, 83, 84, 84, 85] and errors resulting from static correlation[69, 70, 84].

The SIE is closely related to the approximated exchange functionals employed in DFT. It describes the problem that the electrons in DFT not only have repulsive interactions with other electrons as it can be expected, but also interact with themselves. This has several severe implications. The most obvious result is a tendency to favor delocalized, metallic states over local electron configurations[85]. An example for this effect is NiO which appears to be metallic in DFT while an insulating antiferromagnetic electronic structure is found in experiment [57, 86]. In cases where an antiferromagnetic description of the electronic structure is required correction procedures such as broken-symmetry DFT have to be employed[87, 88]. Another effect of the SIE is the fact that band gaps in GGA DFT are generally strongly underestimated[57, 84, 89]. A general solution for this problem does unfortunately not exist. However it was found that hybrid functionals show improved performance for predicting band gaps[84, 90]. A second common approach to minimize the effect of the SIE, especially when dealing with band gaps, is the usage of the DFT+U ansatz[91], where an on-site repulsion U is added as an additional semi-empirical parameter. This on-site repulsion can be understood as a penalty for delocalization of the electrons. Thus, localization of the electrons is enforced. Typical values for this on-site repulsion are of the order of a few eV[91].

A second major problem in present day DFT is static correlation[69, 70, 84]. Similar to the Hartree-Fock theory, KS-DFT in the framework of todays approximate functionals relies only on a single determinant to describe the wave function. Thus, problems can be expected for systems where the wave function is of multi-configurational nature, e.g. due to a number of near-degenerate states. Even though this problem exists both in Hartree-Fock theory and DFT, the reasons are slightly different. While in the former case the Hamiltonian is in principle exact for the non-relativistic case, the problem is caused by an incomplete description of the wave function. In the framework of KS-DFT however the problem is triggered by the necessity to approximate the exact correlation functional[67].

2.6 BASIS SETS AND PSEUDOPOTENTIALS

Having discussed the machinery and problems of wave function based quantum chemical methods and DFT, their implementation remains to be discussed. A central consideration for any type of calculation is the choice of basis set. Basis sets are a set of functions used to approximate the molecular orbitals of the system at hand. From a purely physical perspective the most natural choice would be to express the molecular orbitals as a set of Slater functions, which mimic the shape of the exact 1s hydrogen atomic orbital[56, 63, 67]. However for computational reasons the most common type of basis sets employ Gaussian-type orbitals (GTOs)[56, 63, 67, 92]. GTOs are Gaussian functions of the form

$$\Phi^{GTO} = Nx^l y^m z^n e^{-\alpha r^2} \tag{18}$$

where N is the normalization factor, α the orbital exponent and the exponents l, m and n define the orbital type. The orbital coefficient α is used to determine how compact the orbital is. In the case of a diffuse orbital a small α is used while α is large for a compact orbital. Unfortunately the shape of GTOs differs slightly from those of the Slater-type orbitals (STOs). This problem is avoided by employing a set of Gaussians to form a contracted Gaussian function resembling the features of a STO. A basis set of this type is referred to as STO-LG, where L defines the number of Gaussians employed to mimic the STO. Typically L is at least 3. However the results obtained by employing only one set of contracted Gaussian functions, a so called minimal basis set, are generally poor. This makes it necessary to use more than one set. Basis sets where two or three sets of contracted Gaussian functions are used are referred to as double and triple-ζ, respectively. In split-valence basis sets however only the orbitals occupied by the valence electrons are mimicked by more than one set of contracted Gaussians. Typical examples of a split-valence basis set are the 6-31G double-ζ or 6-311G triple-ζ basis set. In the 6-31G basis set the core electrons are modeled by one contracted Gaussian function consisting of 6 GTOs and the valence electrons by two contracted Gaussians consisting of 3 and 1 GTO, respectively. More often than not it is additionally required to add functions of a higher orbital momentum, e.g. a set of d functions to Li-Ne. These functions are called polarization functions and add an additional flexibility to the wave function by allowing the orbitals to distort from their original symmetry. Additional improvement can be obtained by adding diffuse functions which have a

small orbital coefficient and are thus shallow. These functions are required when modeling anionic systems. While the choice of the basis set is crucial in *ab initio* calculations[93, 94], it is found that DFT is generally less sensible towards the choice of basis set[67, 95]. Similar to Gaussian basis sets are numerical basis sets. Here, the atomic orbitals are represented by a numerical grid centered on the atom instead of Gaussians[67, 96].

In solid state calculations plane waves are often used as a third type of basis sets is often employed when dealing with periodic boundary conditions. A main advantage, giving rise to their popularity when dealing with periodic boundary conditions is the fact that they are already in a form that is conform with the Bloch theorem[57]. Their general form is

$$\Psi_{\mathbf{f}}^{G} = \frac{1}{\sqrt{V}} e^{i(\mathbf{k}+\mathbf{G})\mathbf{r}} \tag{19}$$

where **G** refers to the reciprocal lattice vector. The number of plane waves included in the calculation is defined by the cutoff energy, which defines the maximum kinetic energy of the plane waves used in the calculations.

$$\frac{\hbar^2(\mathbf{k}+\mathbf{G})}{2m_{el}} < E_{cutoff} \tag{20}$$

While their usage is very efficient from a formal point of view it results in practice in a huge number of plane waves that needs to be dealt with. Thus, it is desirable to reduce the size of the required basis set. This means in practice that approximations for the core region are employed and only the valence electrons are modeled explicitly. This lowers the number of required plane-waves significantly[97]. Typical pseudopotentials employed are norm-conserving[97] and ultra-soft pseudopotentials[97, 98]. In the case of norm-conserving pseudopotentials the central condition for constructing the pseudopotential is, that inside the core region, which is defined by a cut-off radius, the norm of the pseudo wave function is equal to the norm of the all electron wave function. In this approximation the exact nodal structure in the core region is no longer of importance, which allows to reduce the number of required plane waves. However, still a significant amount of plane waves are needed to fulfill the condition of norm conservation[97]. By lifting this condition, additional flexibility may be gained, which allows to further reduce the size of the basis set. This is done in the ultrasoft-pseudopotentials. Here the core region no longer needs to be described by the plane wave basis set but is approximated by an effective local

potential. This correction is chosen so that it mimics the effect of norm conservation without using the plane wave basis and thus ensures the correct behavior of the electrons in the valence shell[97].

2.7 TRANSITION STATE SEARCH ALGORITHMS

A central problem in quantum chemistry is the search for transition states in order to judge whether a thermodynamically possible reaction can occur at a significant rate. Over the years a number of algorithms were developed to perform this task. Two of the most commonly used algorithms are the nudged elastic band (NEB)[99, 100] and the linear synchronous transit (LST)/quadratic synchronous transit (QST)[56, 101, 102] methods.

The starting point of the NEB method is a linear pathway between the reactant and product states modeled by a set of intermediate structures along the path. The minimum energy path is then searched by minimizing the forces of the intermediates used to describe the initial path[100].

An alternative algorithm is the LST/QST method. In the LST method the maximum between reactant and product is estimated by a series of single point calculations at a linear interpolation between both points. This is followed by a minimization of the energy perpendicular to the previous LST step using a standard geometry optimization algorithms such as the BFGS algorithm.

The QST algorithm requires in contrast to the LST method already knowledge about the approximate structure of the transition state. This knowledge is used to approximate the reaction path by a quadratic function. This is again followed by an energy minimization orthogonal to the QST step. In many cases the LST and QST methods are used in combination. Typically theses algorithms start with a LST step followed by minimization of the energy orthogonal to the LST path. This guess of the transition state is then used for the subsequent QST step.

The algorithms for transition state searches discussed above allow in many cases to successfully find the transition state and calculate the activation barrier corresponding to the reaction step. The applicability of these methods is however limited to systems where DFT is valid over the whole reaction coordinate. In cases where this is not the case the calculated activation barriers are likely to be wrong. Such a situation can be envisaged among others when the minimum energy path contains a crossing between two electronic states, so called interstates'

crossings. The multi-reference character of the wave function is small in cases where the transition between the two electronic states employs an avoided crossing with a strong coupling between the two states, which results in sufficiently large energy gap. Thus, a DFT proper single-determinantal wave function is sufficient and DFT may still be employed[103]. In the cases where this coupling is weak, the correct wave function close to such interstates' crossings is often multi-configurational in nature. This renders the single-determinant wave function ansatz employed in KS-DFT insufficient. Thus, an alternative procedure is required that build on the DFT proper intermediate states to estimate the activation barriers for such systems.

When dealing with bond formation reactions from a bi-radical state such as in the OER discussed in the present work the coupling between the states is expected to be small even in the case of an avoided crossing. This renders DFT inapplicable for modeling the transition state for the reason discussed above. The procedure used in the present work employs the force constants of the vibrational modes of the di-oxo and μ-peroxo intermediate associated to the O-O bond formation. In paper II an alternative procedure avoiding these problems by relying only on the validity of the reactant and product states was proposed. Assuming a high density of states, which is equal to $E_a \ll h\nu$, and thus the influence of the anharmonicity to be negliable, the activation barrier can be estimated from the crossing of the harmonic oscillators plotted from the force constants of the relevant modes. An analytical expression for this procedure is arrived at from the effective harmonic oscillators of product

$$E_{Prod} = \frac{k_{Prod}}{2} x^2 \tag{21}$$

and reactant

$$E_{React} = \frac{k_{React}}{2} (x - \Delta x)^2 + D \tag{22}$$

Here D is equal to the energy difference between reactant and product, i.e. D=-ΔE. This definition implies that an exothermic reaction step corresponds to a positive D. Δx is the difference between the corresponding bond lengths in the reactant and product states ($\Delta x = x_{React} - x_{Prod}$). From $E_{Prod} = E_{React}$ follows

$$x_{TS} = -\frac{k_{React}}{2\gamma} \Delta x \pm \sqrt{(\frac{k_{React}}{2\gamma} \Delta x)^2 + \frac{k_{React}}{2\gamma} (\Delta x)^2 + \frac{D}{\gamma}} \tag{23}$$

and with

$$\gamma = \frac{k_{Prod} - k_{React}}{2} \tag{24}$$

the bond length in the transition state can be obtained. With this knowledge, the corresponding activation barrier becomes

$$E_a = E_{Prod}(x_{TS}) - D \tag{25}$$

The activation barriers obtained by this method can be expected to present an upper bound of the real activation barrier. This is because here the energy of the actual crossing between the states is approximated. In reality it is likely that an avoided crossing with a possibly small coupling between the states can be found. This results in a lower activation energy.

3 COMPUTATIONAL DETAILS

3.1 MOLECULAR SYSTEMS

The molecular model catalyst shown in Figure 2 was employed in the present work. The dimer was inspired by PS II[24, 25] and other related biomimetic molecular catalysts[38, 39, 41–44]. It consists of two manganese atoms in an octahedral ligand field, bridged by two μ-OH units. The model dimer is terminated by two propane dialdehyde (pdial) moieties, which can be obtained from acetylacetonate (acac) ligands by removing the two methyl-groups, and two hydroxo moieties standing trans to the water molecules subject to subsequent (H^+/e^-) abstraction.

The unrestricted spin DFT calculations at the molecular systems were performed with the Gaussian03 code[104] employing the B3LYP hybrid functional[73, 76, 79]. The influence of the exact exchange was evaluated by additional single point calculations at the B3LYP structures employing the BLYP GGA functional[73, 76]. All calculations were performed using the the triple-ζ 6-311++G basis set with diffuse functions on all atoms. Convergence of the wave functions was achieved using Pulay mixing[105]. In cases where no convergence could be achieved the quadratic convergence scheme[106] was used

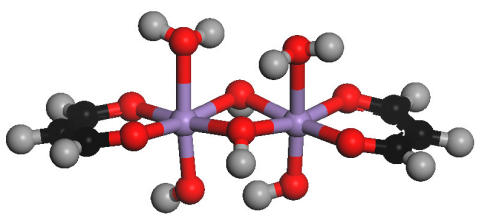

Figure 2: The molecular manganese dimer model complex employed in the present study is depicted. The $Mn_2(OH)_2$ core is terminated by two hydroxo moieties and two pdial groups.

instead. Solvent effects, entropy and zero point energy were assumed to be negligible. The redox reaction steps were modeled employing the tyrosine (TyrOH) tyrosyl radical ($TyrO^{\bullet}$) redox couple as electron and proton sink.

3.2 SURFACE REACTIONS

The electrocatalytic reactions on surfaces were modeled using periodic boundary conditions and a simple test rig embedding. A detailed discussion of the test rig can be found in Section 3.4. All DFT calculations on this surface model system were performed using the CASTEP code[107] as implemented into the Materials Studio suite[108]. A PBE[75] GGA functional in combination with a Γ-point k-point set and a cut-off energy of 400 eV was used. The core electrons were modeled by an ultrasoft pseudopotential[98]. The convergence of the Self Consistant Field (SCF) procedure was aided by a smearing of 0.1 eV. Convergence of the SCF was assumed for an energy change below 10^{-6} eV/atom. The geometry of the test rigs was relaxed employing a BFGS algorithm, which is an implementation of the quasi-Newtonian optimization method. Convergence was assumed for a difference in the total energy below $2 * 10^{-5}$ eV/atom combined with a maximum force of 0.05 eV/Å and a maximum displacement of 0.002 Å. In cases were a cell optimization was performed a Pulay pressure below 0.1 GPa was required. All required molecules were modeled employing the above specifications and a supercell of the size of 10 Å x 10 Å x 15 Å. Similar to the molecular system the TyrOH/$TyrO^{\bullet}$ redox couple was used as reference.

3.3 ACTIVATION BARRIERS

The activation barriers presented here are estimated applying the procedure described in Section 2.7. In case of a molecular embedding, the force constants are extracted from the Gaussian03 calculations after identification of the relevant vibrational modes.

When considering the $MgO_x(OH)_y$ embedding, the force constants were extracted from additional Dmol^3 [96, 109] calculations in order to reduce the computational effort. All energy differences and O—O distances were taken from CASTEP calculations. The Dmol^3 calculations were performed employing the

PBE[75] GGA functional, a Γ-point k-point set and a double-ζ numerical basis set with polarization functions (DNP). The core electrons were approximated with a hardness conserving pseudopotential[110]. The convergence of the SCF was aided by a smearing of 0.005 Ha and convergence was assumed for an energy change below 10^{-6} Ha. Convergence of the geometry was assumed for a maximum force of 0.002 Ha/Å, a maximum displacement of 0.005 Å and an energy change below 10^{-5} Ha.

3.4 THE TEST RIG EMBEDDING

The OER on surfaces is modeled on the test rig embedding shown in Figure 3. It consists of a 2 monolayer thick 1-dimensional wire containing in total 8 $MgO_x(OH)_y$ units where the two central $MgO_x(OH)_y$ units are replaced by the transition metal oxide catalysts. The test rigs are separated by 7 Å of vacuum in order to avoid interactions. The oxidation states are adjusted by hydrogenation of the oxo groups standing trans to the adsorbed water molecules subject to water oxidation, i.e. hydroxo groups are exchanged for oxo-moieties and vice versa. A similar rig embedding was successfully employed by Johnsson-Waas et al.[111].

In contrast to the molecular model system, which reflects in principle a realistic situation that can be envisaged in molecular OER catalysts, the periodic boundary conditions represent only an approximate surface model. The $MgO_x(OH)_y$ embedding was chosen for two main reasons. First, it significantly

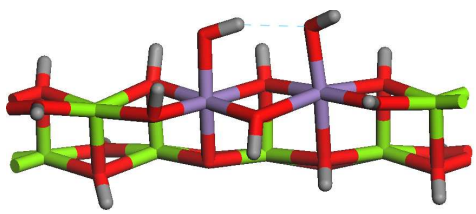

Figure 3: The test rig employed to study electrocatalytic reactions on surfaces is depicted. The rig consists of a 1-dimensional 2 monolayer thick wire of 8 $MgO_x(OH)_y$ units. The two central magnesium atoms are replaced by the transition metal oxide catalyst.

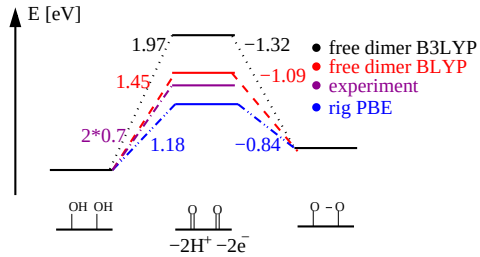

Figure 4: A comparison between the results obtained for Mn(III-V) dimer embedded into the $MgO_x(OH)_y$ test rig and a molecular embedding is shown. Both systems are compared to recent experimental findings on γ-MnOOH[18, 19].

reduces the computational costs of modeling by reducing the size of the model system. Despite the obvious differences between the 1-dimensional $MgO_x(OH)_y$ embedding and situations found in a realistic electrocatalysts, good performance of the model may be expected assuming a purely local chemistry.

The relevance and accuracy of the test rig embedding is discussed by comparison of the $(Mn(IV)—OH)_2$- $(Mn(V)=O)_2$- Mn(IV)-O-O-Mn(IV) reaction sequence for a molecular and a test rig embedded Mn(III-V) dimer candidate catalyst. The results of this comparison are shown in Figure 4. Despite quantitative differences between the two embeddings, i.e. the two (H^+/e^-) oxidation steps at the free molecular model system is found to be 1.45 eV versusTyrOH/TyrO$^\bullet$ compared to 1.18 eV for the rig model qualitative agreement can be claimed. It is also gratifying to note that, assuming solvent effects and differences between the uncorrected energies used here and the Gibbs Free Energies to be negligible, the calculations are in qualitative agreement with recent experimental findings for water oxidation at a MnOOH catalyst[18, 19].

The quantitative differences between the rig and the molecular embedding can partially be attributed to the differences in the type of embeddings. The $MgO_x(OH)_y$ embedding only allows for ionic interactions with the active sites. In case of the molecular systems, interactions from the conjugated π-electron system of the pdial ligand into the d_{xz} and d_{yz} orbitals are possible. These contributions can be expected to compete with the partial double bond character of the Mn(V)=O bond, which in turn weakens the double bond character. As a result a less favorable Mn(IV)-O$^\bullet$ bonding situation is found, resulting in a higher energy cost for the redox step (see Figure 4).

3.5 THE CHOICE OF ELECTRONIC STRUCTURE

As discussed in Section 2.5, DFT is limited to problems that can be described by a single-determinantal wave function[69, 70, 84]. While many problems addressed in chemistry show a large enough gap between the highest occupied molecular orbital (HOMO) and lowest unoccupied molecular orbital (LUMO) orbitals ensuring the required single-reference character of the wave function, this is not the case for the systems at hand. An additional complication is introduced into the manganese dimer by the known antiferromagnetic coupling between the manganese atoms[112–115]. This is problematic for two reasons. First of all it is likely that more than one electronic configuration accounts for a possible antiferromagnetic ground state. Thus, the wave function is expected to be of multi-configurational nature which can not be handled by KS-DFT. A second problem arises from the SIE enforcing a delocalization of the d electrons which may result in a metallic instead of the physically correct antiferromagnetic solution. The latter problem can in principle be dealt with by using a hybrid functional in case of the molecular systems or a DFT+U approach for the solid state calculations. The former problem requires explicit treatment of the static correlation effects. While in *ab initio* quantum chemistry such a type of problems may be attempted to be solved employing a multireference method, no analogous standard methodology exists in DFT. However, even in case of the molecular situation the *ab initio* methods offer no remedy since despite attempts to apply this methodology to transition metal complexes[116, 117] they can still be regarded as too complicated due to the size of the active space necessary to describe the wave function correctly.

A second alternative to treat antiferromagnetic coupling is the procedure introduced by Noodleman et al.[87, 88, 118, 119] which relies on a broken symmetry DFT ansatz. This procedure was considered, but is not applied here. Instead a simpler but also more approximative procedure was employed.

By applying Hund's rule to the transition metal ions discussed in the present work a high spin configuration a high spin configuration is arrived at. The inherent multi-configurational nature of a possible antiferromagnetic coupling, as it can typically be found in manganese dimers, is cured by assuming a ferromagnetic coupling between all unpaired electrons. As a result of these two assumptions a KS-DFT proper single determinantal wave function is arrived at.

Additionally a reduction in the DFT inherent SIE can be expected due to the artificial localization of the unpaired electrons.

The error of such an assumption can be considered to be small since the energies involved in magnetic coupling are generally small compared to reaction energies. As an example the Neél temperature of antiferromagnets is in most cases far below 1000 K[120, 121], which would correspond to an error of approximately 0.1 eV. Hence, the robustness of the results speaks in favor of choosing the high-spin ferromagnetic state in all cases although it introduces an additional methodological uncertainty.

While the electronic structure of the 3d transition metals can be treated by assuming high spin and ferromagnetic coupling between unpaired electrons, this is no longer possible for heavier transition metals such as iridium. These elements are experimentally known to only show low spin configuration[121]. Consequently a low spin configuration was chosen in the calculations.

3.6 THE TYROSINE REFERENCE

In contrast to most other studies[47, 48, 122, 123] on water oxidation, where the HER is chosen as a proton and electron sink, the TyrOH/TyrO$^\bullet$ redox reaction is employed here throughout the whole work. The choice of reference is in principle arbitrary and any system capable of removing one (H^+/e^-) couple at a time may be used. While the choice of the TyrOH/TyrO$^\bullet$ redox couple might at the first glance seem somewhat eccentric it is partly inspired by PS II, where this redox system is possibly involved in the (H^+/e^-) abstraction during the water oxidation cycle[28, 124, 125]. A second more important reason is the similarity of the redox potentials for water oxidation and the TyrOH/TyrO$^\bullet$ couple, which allows for a much simpler interpretation of the results. Indeed, the redox potential of the TyrOH/TyrO$^\bullet$ couple can be found at approximately 0.94 V versus normal hydrogen electrode (NHE)[126, 126, 127], which is close to the 1.23 V relative to the NHE at pH 0 for water oxidation. While this is still approximately 0.3 V below the actual onset of the OER it must be remembered that these potentials are only valid in the case of all reactions occurring in aqueous solution. In the present theoretical study the actual water oxidation steps are modeled neglecting all solvent effects. Thus, single H_2O molecules in vacuum are the substrate for water oxidation. Therefore, when comparing the obtained results with

redox potentials in aqueous solutions, the energy costs for transferring liquid water into the gas phase must be added. Furthermore it is assumed that the minus in entropy resulting from the loss of translational and rotational degrees of freedom and gain in binding energy when adsorbing a water molecule at a free catalytic site cancel, i.e.

$$H_2O_{(g)} + TM^* \longrightarrow TM - OH_2 \qquad \Delta G^0 \approx 0 \tag{26}$$

Based on this assumption the total free energy for the abstraction of four (H^+/e^-) couples at the TyrOH/TyrO$^\bullet$ potential from a transition metal site comes approximately out to be

$$4eE^0_{TyrOH/TyrO^\bullet} = 3.76\ eV \tag{27}$$

When comparing this to the thermodynamic limit of

$$\Delta G^0_{OER} \quad = \quad 4eE^0_{OER} \quad = \quad 4.92\ eV \tag{28}$$

the TyrOH/TyrO$^\bullet$ system comes out to be not sufficient to drive the OER. In the present set of calculations the energy costs for transferring liquid water into the gas phase needs to be added, due to the neglect of solvent effects. This accounts for approximately 2*0.5 eV[128]. Thus, the resulting free energy change for the TyrOH/TyrO$^\bullet$ redox couple becomes 4.76 eV ($\widehat{=}$1.19 V) which is comparably close to 4.92 eV. It can thus be expected that the TyrOH/TyrO$^\bullet$ potential is approximately equal to the onset energy of water oxidation.

An additional beneficial effect resulting from the choice of the TyrOH/TyrO$^\bullet$ redox couple is the approximate cancellation of errors resulting from solvent effects, entropy and zero-point energy for the electrochemical steps. This cancellation can be understood by applying the corresponding Born-Haber cycle shown in Figure 5. In the Born-Haber cycle the oxidation steps occurring in aqueous solution are split into three steps. These steps comprise the conversion of the solvated reactants into gas phase (step 1), the chemical reaction (step 2) and the solvation of the products (step 3). In this cycle, only the energy difference for step 2 is explicitly modeled by DFT. Due to the similarities between the reactants and products of both the TyrOH/TyrO$^\bullet$ redox couple and the intermediates in water oxidation, cancellation of errors from solvent effects, entropy and zero-point energy may be expected. As a result the reaction energies of the water oxidation steps

$$Mn - OH_{2(ads)} + TyrO^\bullet \longrightarrow Mn - OH_{(ads)} + TyrOH_{(g)} \qquad \Delta E_1 \tag{29}$$

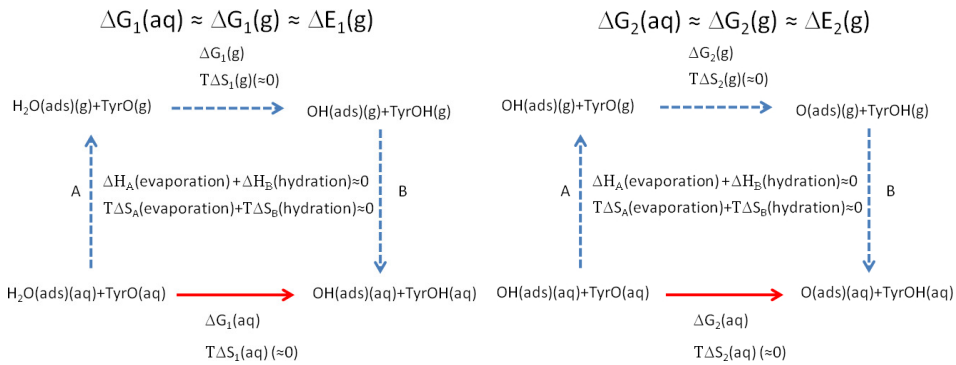

Figure 5: The Born-Haber cycle describing the electrochemical reaction step in solution by an equivalent reaction path following a 3 step mechanism is depicted. The equivalent reaction steps comprise the conversion of the solvated reactants into gas phase (step 1), the chemical reaction (step 2) and the solvation of the products (step 3).

and

$$Mn - OH_{(ads)} + TyrO^{\bullet} \longrightarrow Mn = O_{(ads)} + TyrOH_{(g)} \qquad \Delta E_2 \qquad (30)$$

become approximately similar to the change in the Gibbs Free energy at, i.e. $\Delta G_1^o \approx \Delta E_1^o$ and $\Delta G_2^o \approx \Delta E_2^o$.

3.7 CONVERGENCE TEST

A critical parameter in the accuracy of any calculation is the necessary compromise between the computational costs and a sufficiently large basis set and in the case of periodic boundary conditions calculations the k-point set. In what follows the accuracy of the chosen parameters will be discussed.

Starting the discussion with the CASTEP plane wave calculations, the accuracy of the calculations is defined by the k-point set and the cutoff energy of the plane wave basis set. A convergence test for the choice of cutoff energy and the

Table 1: The convergence of the k-point and basis sets are summarized. The k-point set and plane-wave cutoff energy convergences is discussed for the Mn(III-V) dimer embedded into the $MgO_x(OH)_y$ embedding employing the O-O bond formation step as benchmark reaction. The convergence of the Gaussian basis set is discussed with respect to the oxidation of Mn(IV)-OH to Mn(V)=O at a $Mn(pdial)_2(OH)_2$ monomer using the B3LYP xc-functional.

$MgO_x(OH)_y$ embedding				$Mn(pdial)_2(OH)_2$	
k-point set		cutoff energy			
k-points	E [eV]	E_{cutoff} [eV]	E [eV]	basis set	E [eV]
1x1x1	-0.84	300	-0.90	6-311++G	0.84
2x1x1	-0.84	350	-0.84	6-311+G(d)	0.97
4x1x1	-0.84	400	-0.84	6-311+G(d,p)	0.95
		450	-0.84		
		500	-0.84		

k-point set can be found in Table 1. The convergence is tested for the O-O bond formation step at a Mn(III-V) dimer embedded into the $MgO_x(OH)_y$ rig.

$$2Mn(V) = O \longrightarrow Mn(IV) - O - O - Mn(IV) \tag{31}$$

The cutoff energies are varied between 300 eV and 500 eV at a Γ-point k-point set. Furthermore k-point sets from 1x1x1 up to 4x1x1 at a 400 eV cutoff are compared. A minor change in energy from -0.90 eV to -0.84 eV can be seen when increasing the cutoff from 300 eV to 350 eV, above 350 eV the reaction energy is found to be constant. Thus, an increase of the basis set beyond 350 eV will not increase the accuracy of the calculations. In case of an increased k-point set no differences were found when increasing it from a Γ-point k-point set to a 4x1x1 set (see Table 1). This result is not unexpected considering the purely ionic nature of the $MgO_x(OH)_y$ embedding. This type of embedding allows only for long range ionic interactions. The band dispersion, described by the k-points can therefore be assumed to be negligible due to the missing bonding and antibonding interactions between the unit cells. This results in the insensitivity of the reaction energy with respect to the chosen k-point set found here.

In case of the Gaussian03 calculations the 6-311++G basis set was employed. Even though DFT is not as sensible as *ab initio* quantum chemical methods towards the size of the basis set, the complete neglect of polarization functions may still be a major source of errors. This effect is presumably especially large for the description of the Mn(V)=O bond, which would profit the most from the additional flexibility of the wave function introduced by polarization functions. The convergence with respect to the inclusion of polarization functions is summarized in Table 1. The test is performed for a $Mn(pdial)_2(OH)_2$ monomer applying the Mn(IV)-OH to Mn(V)=O oxidation step as benchmark reaction. While a minor increase in the oxidation energy can be found upon inclusion of polarization functions, the effect is still small compared to all other sources of errors. Thus, the choice of a 6-311++G basis set can be considered as sufficient for the qualitative accuracy needed in the present study.

4 WATER OXIDATION

In what follows the contents of the publications attached to this work will be reviewed. In Section 4.1 the fundamental OER mechanism is discussed for a molecular manganese dimer. This discussion is based on the results presented in the Publications II and III. The insights gained from the mechanistic study are then applied in Section 4.3.1. The first part of that section comprises a comparative study of the reactivity of a series of 3d TM oxides embedded into the $MgO_x(OH)_y$ test rig. This part is based on the Publications IV and V. Additionally a comparison of the performance of manganese oxide with IrO_2, which can be found in Paper VI, is included. In Section 4.3.3 the implications of the Publications IV and V concerning to the possibility of improving the performance of the homonuclear OER catalysts by mixing transition metals are presented. The idea of mixed TM oxide catalysts is then generalized for mixed oxidation state systems in Section 4.3.4 (Paper VI). In order to test the validity of the binuclear paradigm, a discussion concerning recent experimental findings on IrO_x (Section 4.3.2) and RuO_2 (Section 4.2) is added. These sections are based on the Papers I and VII.

4.1 THE BINUCLEAR MECHANISM

In literature two main mechanisms for water oxidation are discussed. These mechanisms differ with respect to the O-O bond formation step. In case of the mononuclear mechanism, supported by several groups[45, 47, 48, 122, 129, 130], the O-O bond formation is facilitated by the reaction between a bulk water molecule and a surface TM=O species. This results in the formation of a TM-OOH intermediate. The binuclear OER mechanism in contrast requires two neighboring surface TM=O moieties to form the O-O bond. In this intramolecular reaction step a μ-peroxo bridged species is formed. Such a binuclear mecha-

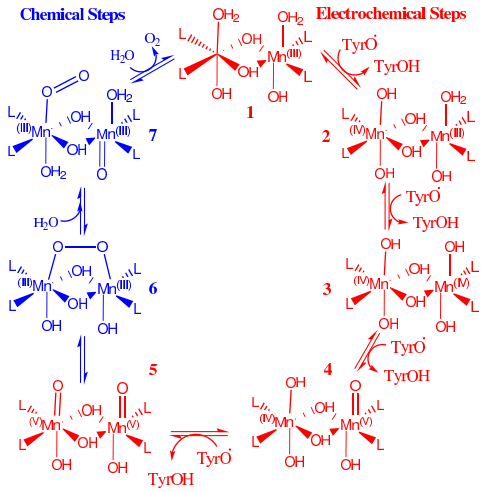

Figure 6: The assumed binuclear OER mechanism is illustrated. The catalytic steps can be divided into a series of electrochemical (red) and chemical steps (blue).

nism was first proposed several decades ago by Bockris et al.[11] and is considered to be relevant by a few groups[18, 19, 131].

One of the aims of the present work is to evaluate and gain a comprehensive understanding of the binuclear OER mechanism. A typical reaction sequence is shown in Figure 6. In the binuclear mechanism the reaction sequence is divided into a series of electrochemical steps comprising the abstraction of in total 4 (H^+/e^-) couples (see red reaction steps in Figure 6). The oxidation steps are followed by the recovery of the catalytic sites in a series of purely chemical steps (see blue reaction steps in Figure 6). The full binuclear mechanism is studied in the present work employing a simple di-μ-OH bridged manganese dimer model catalyst.

Equivalent to the mononuclear mechanism[47, 48], the binuclear OER mechanism starts with the oxidation of a Mn(III)-OH_2 species (intermediate *1*) in two consecutive steps to Mn(V)=O via Mn(IV)-OH. In contrast to the mononuclear mechanism, where the formation of one Mn=O moiety is sufficient, the oxidation sequence is repeated for a neighboring Mn(III)-OH_2 group. Having oxidized the Mn(III)-OH_2 all the way up to Mn(V)=O (see structure *5*), the maximum numbers of possible (H^+/e^-) couples is removed and the catalyst needs

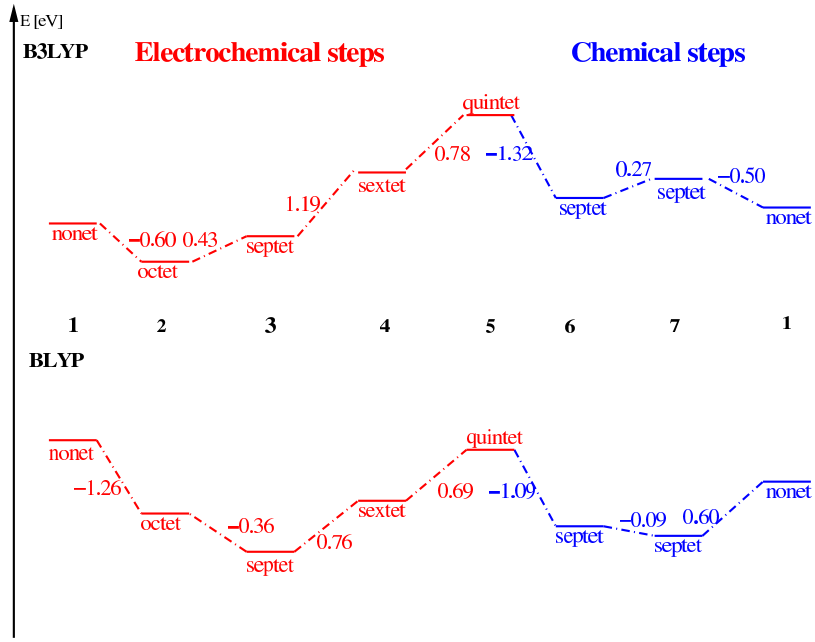

Figure 7: The energy profile of the high spin path employed to model the binuclear water oxidation mechanism is shown for B3LYP (top) and BLYP (bottom). The colors show the division into electrochemical (red) and purely chemical steps (blue).

to be recovered. Since the aim of the water splitting is to obtain hydrogen or similar (H^+/e^-) reducing equivalents, in principle any reaction that allows for the removal of the oxo moieties would be suitable. Indeed the energy efficiency of the whole water splitting reaction could be increased by co-production of other valuable chemicals such as oxirane discussed in Paper I. In the present work catalyst recovery is assumed by a three step O_2 evolution mechanism. The first step comprises a purely chemical intramolecular O-O bond formation step resulting in the formation of a μ-bridged intermediate (structure *6*). This is followed by the subsequent replacement of the Mn(IV)-O_2 bonds with water, finally recovering the starting point, structure *1*, again.

The energetics of this reaction mechanism obtained for a DFT proper high spin path are shown in Figure 7 for the B3LYP hybrid and the BLYP GGA functional.

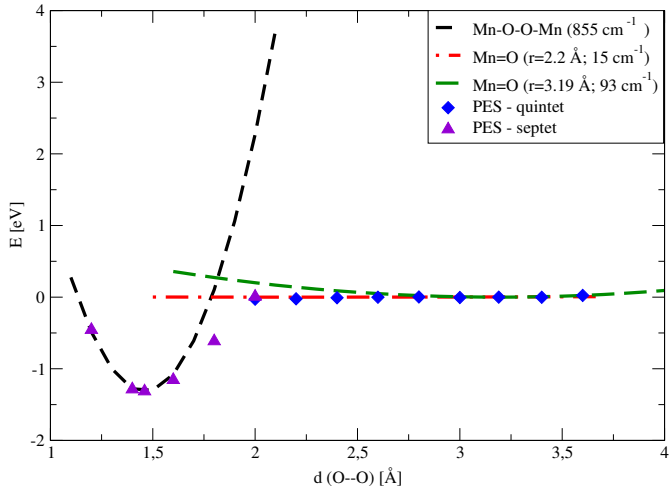

Figure 8: The harmonic oscillators used to approximate the activation barrier of the O-O bond formation step are depicted. For comparison a constrained geometry optimization at discrete points on the potential energy surface is added.

At the B3LYP level of theory, the oxidation of two d^4 Mn(III)-OH_2 moieties (structure *1*) to form d^3 Mn(IV)-OH (structure *3*) appears to proceed approximately at the TyrOH/TyrO$^\bullet$ energy, i.e. the first oxidation step is exothermic by 0.60 eV followed by a second step which is endothermic by 0.43 eV. Tracking the B3LYP energy profile further, two d^2 Mn(V)=O moieties (structure *5*), which are assumed to be in a quintet spin state, are formed. These two oxidation steps are found strongly endothermic by in total 1.97 eV, i.e. the first step is endothermic by 1.19 eV followed by a second step endothermic by "only" 0.78 eV versus TyrOH/TyrO$^\bullet$. Having arrived at this highly activated intermediate, the subsequent O-O bond formation is strongly exothermic by 1.32 eV. The final release of $^3O_2$ is, in contrast to the study by Baik et al. at a ruthenium dimer[130] but in agreement with experiment[132], found to be unproblematic. The first replacement of a Mn-O_2 bond is endothermic by 0.27 eV followed by an exothermic final O_2 release step.

Considering the discussed energy profile, the critical steps in the binuclear mechanism are certainly the oxidations of Mn(IV)-OH to Mn(V)=O and the subsequent O-O bond formation. The former reaction is decisive for the overpoten-

tial while the latter is required to recover the catalytic sites. In case of the present Mn(III-V) model system the O-O bond formation was found highly exothermic. Thus, this reaction should in principle be unproblematic. However, since this step is purely chemical in nature a significant activation barrier can still block the O-O bond formation despite the favorable thermodynamics reported here. The energetics of both reaction steps indeed depend on the relative stability of the di-oxo intermediate *5*. In the case of a highly reactive intermediate, which is equal to a more Mn-O$^{\bullet}$ like electronic structure, the O-O bond formation is strongly favored at the price of a high overpotential. However, in cases where the di-oxo intermediate is too stable the O-O bond formation is hindered and consequently the catalyst unable to recover the catalytic sites via a binuclear OER mechanism.

So far the OER has only been discussed from a thermodynamic perspective. In the present work activation barriers are estimated employing the harmonic oscillator approximation described in Section 2.7. The relevant modes contributing to the O-O bond formation were extracted from the calculated infra red (IR) spectra of the di-oxo intermediate *5* and the μ-peroxo intermediate *6*. In the case of the di-oxo structure the relevant mode was found at 93 cm^{-1} with a force constant of only 4.5 N/m. For the μ-peroxo bridged intermediate the vibrational mode at 855 cm^{-1} with a force constant of 395 N/m was found. By plotting the resulting harmonic oscillators the activation barrier was estimated from the crossing of the curves to be 0.3 eV (see Figure 8). Considering the low force constants, which are a result of the high flexibility of the catalyst, and the resulting low activation energy it can be expected that the O-O bond formation proceeds without significant barrier for this molecular model catalyst. Interestingly this activation barrier is similar to what has been proposed for the intramolecular O-O bond formation in PS II[133].

In case of surface OER electrocatalysts, as they will be discussed later, hybrid functionals can no longer be used due to their high computational costs. Thus, one has to rely on the applicability of pure GGA functionals. A comparison of the energetics of the full binuclear mechanism applying both the B3LYP hybrid functional and the BLYP GGA functional is shown in Figure 7. It is gratifying to note that both functionals are in qualitative agreement for the central reaction steps. This means similar trends for the oxidation of Mn(IV)-OH to form Mn(V)=O and the subsequent O-O bond formation between two neighboring Mn(V)=O moieties are found. The comparably large differences in the num-

Table 2: Summary of important bond lengths and Mulliken spin densities of the di-hydroxo (structure *3*), the di-oxo (structure *5*) and the μ-O_2 (structure *6*) intermediates. All values were obtained with the B3LYP hybrid functional.

		bond lengths [Å]			spin densities	
structure	spin	Mn1-O1	Mn2-O2	O-O	O1	O2
$(Mn{-}OH)_2$	septet	1.89	1.82			
$(Mn{=}O)_2$	quintet	1.78	1.80	3.19	-0.85	-0.90
	nonet	1.85	1.89	3.24	1.11	1.10
Mn-O-O-Mn	septet	1.89	1.89	1.46	0.20	0.20

bers can be understood considering the possible mesomeric structures of the Mn(V)=O intermediate:

$$Mn(V) = O \leftrightarrow Mn(IV) - O^{\bullet} \tag{32}$$

In case of BLYP a more double bonded Mn(V)=O like intermediate is formed. This is indicated by the comparably lower spin densities of only 0.24 and 0.43 at the oxygens. B3LYP in contrast shows already in the case of the lower lying quintet spin state, which would in principle allow for a double bond description of the Mn(IV)-$O^{\bullet}$ bond, nearly pure radical character on the oxygens (see Table 2). These differences are also reflected in the energy gap between the quintet spin state and the nonet spin state which enforces a pure radical Mn(IV)-$O^{\bullet}$ state. In case of B3LYP this differences found to be only 0.36 eV compared to 0.83 eV for BLYP.

Major qualitative and quantitative differences can also be found for the oxidation of the Mn(III)-OH_2 moieties to Mn(IV)-OH and the O_2 release step. In case of the former B3LYP predicts the 2 (H^+/e^-) oxidation to occur approximately at the TyrOH/TyrO$^{\bullet}$ energy, while it is found to be exothermic by in total 1.62 eV for BLYP. This large difference can be attributed to the erroneous description of weakly adsorbed molecules, such as water[134], and a severe underestimation of band gaps due to the SIE[57, 84, 89] when employing a GGA. Similar effects can also be expected for the final O_2 release step.

4.2 IS A BINUCLEAR MECHANISM REALISTIC?

A test case for the binuclear mechanism is RuO_2. In the present work, the OER and the oxidation of ethene at RuO_2 are studied by a combined DFT and experimental approach. In case of a Cl^- free solution, the OER is found at a low overpotential and ethene is oxidized to CO_2. When adding chloride to the solution the OER is shifted to higher overpotentials. Additionally no CO_2 is formed, but ethene is oxidized to oxirane at a potential where O_2 evolution would be possible. Assuming a binuclear mechanism for both the oxidation of ethene to CO_2 and the OER, chloride can be understood to block the neighboring reaction sites. It was indeed found in DFT calculations that the full oxidation of ethene proceeding via a binuclear mechanism is strongly favored compared to the formation of oxirane. However, by blocking the neighboring sites with chloride, ethene can only be oxidized to oxirane, since this reaction requires, in contrast to the full oxidation, only a single Ru=O site. Similarly, an intramolecular O-O bond formation between two Ru=O is no longer possible. Thus, these results suggest, that a binuclear mechanism for the OER on RuO_2 at lower overpotentials is likely.

4.3 IMPLICATIONS OF A BINUCLEAR MECHANISM

4.3.1 Homonuclear Catalysts

In what follows the insights gained for a molecular Mn(III-V) dimer will be used to understand the reactivity of a series of 3d transition metal oxides. The

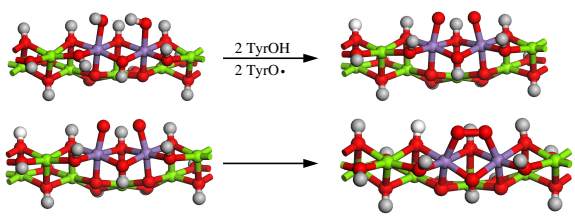

Figure 9: The $MgO_x(OH)_y$ rig model and the reaction steps used as descriptors for the performance of the candidate catalysts towards water oxidation are shown.

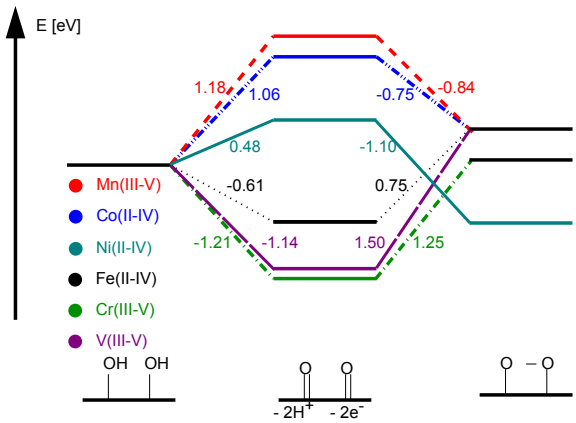

Figure 10: The energy profiles of the studied TM oxides for the oxidation from TM-OH to TM=O followed by the intramolecular formation of the μ-peroxo bridge are shown. All energies are in [eV] and the TyrOH/TyrO• couple is used as reference system.

catalysts are studied employing the $MgO_x(OH)_y$ test rig model system described in Section 3.4 and shown in Figure 9. The oxidation of 2TM-OH to 2TM=O and the subsequent O-O bond formation are employed as descriptors for the performance of the candidate catalysts (see Figure 9).

In Figure 10 the results for V(III-V),Cr(III-V), Mn(IIII-V), Fe(II-IV), Co(II-IV) and Ni(II-IV) are depicted. Interestingly the pure transition metal oxides are found to belong to two distinct classes, which emerge at the TyrOH/TyrO• oxidation potential (see Figure 10). This behavior is not unexpected considering the overall trends in reactivity in the periodic table[121], i.e. high oxidation states are favored for early transition metals, while late TMs prefer lower ones. Indeed V(III-V) and Cr(III-V) are found to belong to one class and Co(II-IV) and Ni(II-IV) to a second class. The former set ([-/+] class) shows stabilization upon formation of the TM=O bond from TM-OH, i.e. the oxidation step is found exothermic with respect to the TyrOH/TyrO• energy. The exothermic oxidation step is mirrored by an endothermic O-O bond formation. The latter class of oxides ([+/-] class) shows opposite behavior. Here, the formed TM=O/TM-O• moieties are more unstable compared to the TyrO• radical, resulting in an endothermic oxidation step, followed by an exothermic O-O bond formation. While the very

early TMs V(III-V) and Cr(III-V) are of [-/+] type and the late TMs Co(II-IV) and Ni(II-IV) of [+/-] type, one could expected Mn(III-V) and Fe(II-IV), judging from their position in the periodic table, to show intermediate behaviors. However, Fe(II-IV) is found to belong to the [-/+] class and Mn(III-V) to the [+/-] oxides. This somewhat unexpected behavior can be accounted for, considering the fact that different oxidation states are used, which results into the reordering reported here.

The differences in energetics between the two classes can be understood from the differences in the electronic structures of the TM=O intermediates. In Table 3 the Mulliken spin densities and bond lengths of the di-hydroxo, the di-oxo and the μ-peroxo intermediates are summarized. When comparing the bond lengths and oxygen spin densities of the [+/-] group oxides, TM=O bond lengths slightly shorter than those found for a purely single bonded TM-OH intermediate are found. This together with significant spin density at the oxygen (see Table 3) points towards a significant partial radical nature at the oxo moiety. As a consequence of this highly reactive radical intermediate the O-O bond formation is strongly exothermic. However even in the case of [+/-] oxides the TM-$O^{\bullet}$ moieties are stabilized by at least a partial double bond. Indeed, in cases where such a stabilization is not possible the oxidation of TM-OH to form TM-$O^{\bullet}$ can be expected to be very similar to the abstraction of a (H^{+}/e^{-}) couple from H_2O, where no stabilization is possible. Such a case is for example found for the Ti(III-IV) system. Here, the formation of two Ti(IV)-$O^{\bullet}$ from two Ti(IV)-OH is endothermic by 2.53 eV compared to 2.75 eV for the same (H^{+}/e^{-}) abstraction step at two water molecules. The oxo intermediates of the [-/+] class show in contrast to the [+/-] oxides comparably shorter bond lengths. This is accompanied by, except for the Fe(IV)=O intermediate, only negliable spin densities at the oxygens (see Table 3). Thus, the TM=O bonding situation is of a more stable mainly double bond like nature. This results in the strongly endothermic O-O bond formation (see Figure 10).

Returning to the results of the complete binuclear mechanism discussed in Section 4.1, the most critical reaction step is, from a kinetic point of view, the O-O bond formation. Similar to the molecular manganese dimer the activation barriers are estimated employing the harmonic oscillator approximation. Assuming the force constants used to estimate the barriers of the O-O bond formation step to mainly depend on the TM-O bond type but not so much on the transition metal itself, Mn(III-V) and Co(II-IV) may be taken as representatives of the [+/-] class. By employing this approximate procedure an activation barrier of 1.12 eV

Table 3: A summary of characteristic bond lengths and Mulliken spin densities for reactants, intermediates, and products for the considered homo-binuclear transition metal systems is given.

			bond lengths [Å]			Mulliken spin	
metal	structure	spin	M1-O1	M2-O2	O1-O2	O1	O2
V	$(OH)_2$	triplet	1.84	1.96			
III-V	$(=O)_2$	singlet	1.65	1.65	3.12	0	0
	O-O	triplet	1.90	1.90	1.43	-0.08	-0.08
Cr	$(OH)_2$	quintet	1.84	1.93			
III-V	$(=O)_2$	triplet	1.62	1.63	3.12	-0.24	-0.24
	O-O	quintet	1.89	1.89	1.45	-0.12	-0.12
Mn	(OH)2	septet	1.96	1.91			
III-V	$(=O)_2$	quintet	1.79	1.79	2.13	-0.50	-0.50
	O-O	septet	1.96	1.96	1.44	0.14	0.14
Fe	$(OH)_2$	11-tet	1.92	1.86			
II-IV	$(=O)_2$	nonet	1.67	1.67	3.12	0.66	0.66
	O-O	11-tet	1.95	1.94	1.41	0.48	0.48
Co	$(OH)_2$	singlet	1.90	1.88			
II-IV	$(=O)_2$	triplet	1.77	1.77	2.35	0.82	0.82
	O-O	singlet	1.92	1.91	1.43	0	0
Ni	$(OH)_2$	septet	1.87	1.89			
II-IV	$(=O)_2$	nonet	1.74	1.74	3.32	1.48	1.48
	O-O	septet	2.05	2.05	1.33	0.66	0.66

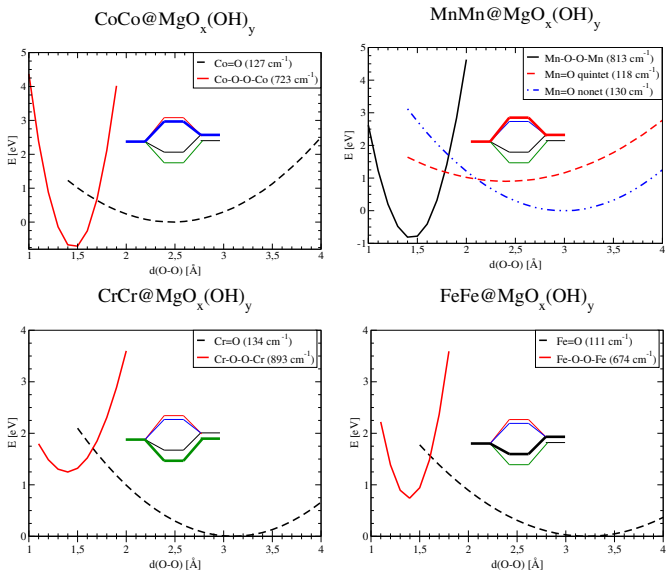

Figure 11: The harmonic oscillator approximation plots used to estimate the activation barriers for the O-O bond formation step on Cr(III-V), Fe(II-IV), Co(II-IV) and Mn(III-V) are shown.

was found for Mn(III-V) and a barrier of 0.64 eV for Co(II-IV) (see Figure 11). Thus, these systems should show good performance in the electrochemical OER, which is indeed also found experimentally[18–20, 22, 135]. While the activation barrier for the cobalt system was estimated directly from the di-oxo ground state, a two step mechanism was assumed in the case of manganese. The first step comprised the breaking of the partial Mn=O double bond to form a pure Mn-O$^{\bullet}$ radical state. This is equal to a transition from a quintet to a nonet spin state. This step was followed by the actual O-O bond formation. The large difference between the activation barriers found for the molecular system and the test rig embedding can be attributed to the rigidity of the latter. In case of the [-/+] catalysts Cr(III-V) and Fe(II-IV) were considered. For these systems an activation barrier of 1.70 eV (Cr(III-V)) and 1.56 eV (Fe(II-IV)) was found (see Figure 11). A two step mechanism as assumed for Mn(III-V) did, due to the higher stability of the TM=O bond, not result in a lowering of the activation barrier. Thus, the

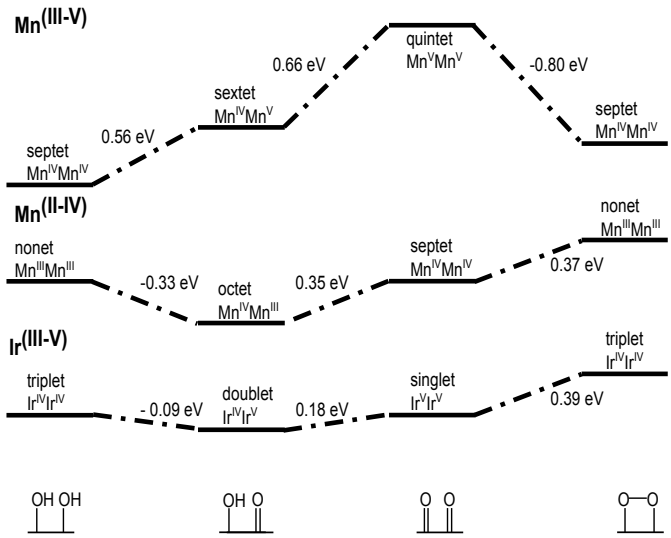

Figure 12: The energy profile of Mn(II-IV) and Ir(III-V) for the key reaction steps in the OER are depicted. Mn(III-V) is added for comparison. Variations from previously reported energies are due to the including of cell optimization in the present set of calculations.

[-/+] systems are expected to show poor performance towards the OER, which is indeed also found in experiment[136].

Until now it was assumed that the onset of oxygen evolution requires manganese in the oxidation state +V. However when simply considering the redox potential of the lower Mn(II-IV) couple, which is at 1.22 V versus NHE[128], the Mn(II-IV) system should thermodynamically be able to evolve oxygen. In Figure 12 the energy profile for the di-hydroxo, oxo-hydroxo, di-oxo, μ-peroxo pathway is reported for the Mn(II-IV) and Ir(III-V) dimers embedded into the $MgO_x(OH)_y$ rig.

Judging from the closeness of the redox potential for the Mn(II-IV) couple to the OER potential, the energy profile of Mn(II-IV) is expected to be approximately thermoneutral for the oxidation steps. Indeed, the exothermicity of 0.33 eV and the endothermicity of 0.35 eV for the two oxidation steps are found to cancel. The subsequent O-O bond formation however is found to be endothermic by 0.37 eV (see Figure 12). The extent to which the energy profile

of the Mn(II-IV) system is close to ideal can be appreciated by comparing with the [+/-] and [-/+] classes of 3d TM oxides (see Figure 10) and IrO_x. In contrast to the [+/-] and [-/+] systems where either a high overpotential is found or the O-O bond formation is unfavorable, the Mn(II-IV) system shows near ideal behavior. This means, a minimal overpotential is combined with a small endothermic μ-peroxo bond formation step (see Figure 12). Such a behavior is also found for IrO_x, which is a well known and very active catalyst for the OER catalyzing the water oxidation reaction at a small overpotential[137, 138]. Assuming the oxidation state responsible for oxygen evolution, in agreement with experiment, to be Ir(V)[139] (see also Paper VII), the Ir(III-V) system may be used to model the OER at this oxide. The results for the Ir(III-V) dimer are shown in Figure 12. Indeed also for iridium the di-hydroxo intermediate is oxidized to di-oxo at approximately the TyrOH/TyrO$^\bullet$ energy level, i.e. the first step is exothermic by 0.09 eV followed by an step endothermic by 0.18 eV. The subsequent O-O bond formation step is endothermic by 0.39 eV.

Considering the similarities between the energetics for Ir(III-V) and Mn(II-IV) the latter should, similar to iridium, catalyze water at a low overpotential. This is however not the case and it is found experimentally, that onset of the OER is at a significantly higher potential for heterogeneous systems[18, 19]. Thus, the O-O bond formation can be expected to be kinetically hindered. Considering the harmonic oscillator approximation applied previously for Mn(III-V), a two step mechanism for partly double bonded systems similar to Mn(V)=O needs to be applied for the Mn(IV)=O system. This mechanism proceeds via the formation of two Mn-O$^\bullet$ intermediates followed by the actual O-O bond formation. While the corresponding vibrational modes contributing to the O-O bond formation can be assumed to only depend on the bond type but not on the transition metal, the breaking of the TM=O bond is dependent on the transition metal and oxidation state. In case of Mn(V)=O the breaking of two partial double bonds was of the order of 0.9 eV. For Mn(IV)=O/Mn(III)-O$^\bullet$ in contrast 2.3 eV were found. This and the additional endothermicity of 0.37 eV of the O-O bond formation renders this step kinetically hindered. Ir(III-V) however is despite a similar endothermicity active towards the OER. This can be understood considering the Mulliken spin densities shown in Table 4. In case of iridium the radical state is already found to be the ground state. Thus, the initial breaking of a partial double bond is not necessary and the activation energy is expected to be small.

Table 4: Summary of all relevant Mulliken spin densities of the di-oxo intermediates for Mn(II-IV), Mn(III-V) and Ir(III-V).

system	spin	TM1	TM2	O1	O2
$(Ir(IV)=O)_2$	singlet	-0.82	0.82	-0.96	0.96
$(Mn(IV)=O)_2$	septet	2.54	2.54	0.52	0.52
$(Mn(V)=O)_2$	quintet	2.42	2.42	-0.48	-0.50

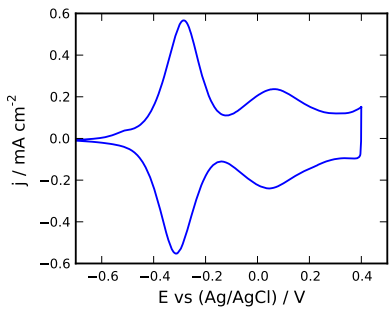

Figure 13: A typical CV of IrO_x measured in 0.1 M KOH at a scan rate of 10 mV/s is depicted. The data are reported versus the Ag/AgCl reference electrode.

4.3.2 A Combined Experimental and DFT View on Iridium Oxide

As a test for the validity of a binuclear mechanism a comparison between experimental findings at IrO_2 and their interpretation in terms of a binuclear mechanism will be presented. In Figure 13 a typical cyclic voltammogram (CV) for IrO_2 is shown. The central feature of the CV are the two peaks at -0.3 V versus Ag/AgCl[1], which corresponds to Ir(III)Ir(III)/Ir(IV)Ir(IV), and 0.05 V versus Ag/AgCl, which shows only approximately 0.7 times the charge of peak 1 and thus corresponds to a partially oxidized Ir(IV)Ir(IV)/Ir(IV)Ir(V) redox couple. In terms of a Ir(III-V) system embedded into the $MgO_x(OH)_y$ test rig environment these redox couples correspond to the oxidation of 2 Ir(III)-OH_2 to Ir(IV)-OH (see Figure 14a) followed by the oxidation of a single Ir(IV)-OH to

1 in saturated KCl: 0.197 versus NHE

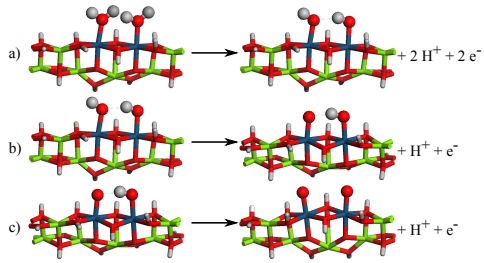

Figure 14: The oxidation steps found in the CV (see Figure 13) interpreted in terms of the test rig embedding are shown. Step a) corresponds to Ir(III)Ir(III)/Ir(IV)Ir(IV), step b) to Ir(IV)Ir(IV)/Ir(IV)Ir(V) and step c) to the onset of oxygen evolution.

Table 5: The Mulliken spin densities of the Ir1(V)=O Ir2(IV)-OH intermediates are shown.

method	U	Ir1	Ir2	O1	O2
PBE		0.84	-0.58	0.86	-0.18
PBE+U	2 eV	0.06	0.7	-0.02	0.14
PBE+U	3 eV	0.1	0.78	-0.02	0.12
PBE+U	4 eV	0.1	0.78	-0.1	0.12

form a Ir(V)=O Ir(IV)-OH dimer intermediate (see Figure 14b). Assuming a binuclear mechanism. Thus, the appearance of a Ir(IV)Ir(IV)/Ir(IV)Ir(V) redox couple preceding the OER is not in contradiction with a binuclear mechanism. In case of a mononuclear mechanism in contrast only one of these highly reactive groups would be required.

Interestingly, GGA calculations show a pure radical nature at the Ir(IV)-OH Ir(V)=O oxo group (see Table 5). Keeping in mind that a radical nature at the oxygen is, at least in the case of manganese[43, 140], a requirement for a mononuclear mechanism, this would be in contradiction to what is found experimentally. However, when curing for the SIE, which is known to be a problem for strongly localized systems, by a GGA+U ansatz, the radical character at the oxo group vanishes (see Table 5). Thus, the mononuclear and binuclear mechanisms are again in agreement in predicting the onset of the OER at a di-oxo dimer, where full radical character is found at the oxygens.

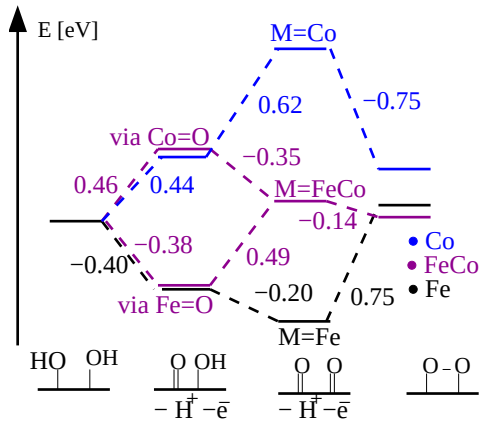

Figure 15: The reaction energetics for hydroxide oxidation and μ-peroxo bridge formation at the hetero-binuclear FeCo sites is depicted. The results for the homo-binuclear Fe and Co sites are included for reference. All energies are given in [eV].

4.3.3 Heteronuclear Water Oxidation Catalysts

Having learned about the existence of two classes of OER catalysts showing opposite energetics, it is tempting to predict mixed TM oxide catalysts which mimic the reactivity of the near ideal IrO_x catalyst. Based on the assumption of purely local chemistry a mixed [+/-] [-/+] TM oxide system can be expected to show such a behavior. This means, the exothermicity in the oxidation of a Fe(III)-OH, V(IV)-OH or Cr(IV)-OH is expected to approximately cancel the high overpotential found for the oxidation of a TM-OH moiety of a [+/-] group oxide. Having one highly reactive and one stable TM=O intermediate, the resulting energetics of the O-O bond are also expected to end up approximately thermoneutral.

This concept is evaluated in detail for the FeCo mixed TM system. The results for the water oxidation reaction at this mixed oxide system are summarized in Figure 15. It is remarkable to which extent the system shows the expected cancellation effect. The 2 (H^+/e^-) oxidation step from the di-hydroxo intermediate to form a di-oxo species is endothermic by only 0.11 eV. Also in the subsequent O-O bond formation step qualitative cancellation resulting in an exothermicity of only 0.14 eV is found.

A central assumption in the design of the mixed transition metal oxide systems is the validity of a local description of the chemistry at the TM sites. When considering the oxidation of the TM-OH intermediates the abstraction of a hydrogen may either occur at the Fe(III)-OH or the Co(III)-OH group in the first step. In both cases the single (H^+/e^-) oxidation steps are found to be in good agreement with the corresponding homonuclear system (see upper and lower branches of Figure 15). This justifies the assumption of a purely local chemistry.

Having understood the mechanics of mixed TM oxides, the concept is applied to the 3d oxides discussed in Section 4.3.1. Based on the findings for the FeCo system, which suggest that the catalytic sites are indeed independent from each other, the electrocatalytic properties of a mixed system may be estimated from the pure oxides by simply adding the energetics for a monomer site up. Thus, in case of the binuclear systems one obtains

$$\Delta E = \frac{E(TM1{=}O) - E(TM1\text{-}OH) + E(TM2{=}O) - E(TM2\text{-}OH)}{2} \tag{33}$$

for the oxidation of the di-hydroxo intermediate to the di-oxo system. The energetics of the O-O bond formation step are estimated correspondingly via

$$\Delta E = \frac{E(TM1\text{-}O_2\text{-}TM1) - E(TM1{=}O) + E(TM2\text{-}O_2\text{-}TM2) - E(TM2{=}O)}{2} \tag{34}$$

The results of this simple estimate are shown in Figure 16.

Consistent with the FeCo system discussed above an improvement of the catalytic performance to the near-optimum is found upon pairing of [+/-] and [-/+] class catalysts. This means all mixed systems considered are close to the origin, where a thermoneutral O-O bond formation is combined with a minimal overpotential for the oxidation of the hydroxo intermediate. However considering the fact that an additional activation barrier needs to be overcome when forming the O-O bond, systems with a net endothermicity for this reaction step may exhibit slow kinetics. Such an effect can be expected for Co(II-IV)V(III-V), Co(II-IV)Cr(III-V) and Mn(III-V)V(III-V).

Due to the approximate nature of the applied procedure a test for its validity is offered. This is done for a set of mixed TM oxides by explicit calculation of the energetics of both reaction steps. The results are shown in Figure 17. It is gratifying to note the degree to which extend the compared systems are, despite some scatter, in agreement. The largest deviation between estimated and calculated values are of the order of only 0.3 eV for the Ni(II-IV)Fe(II-IV) and

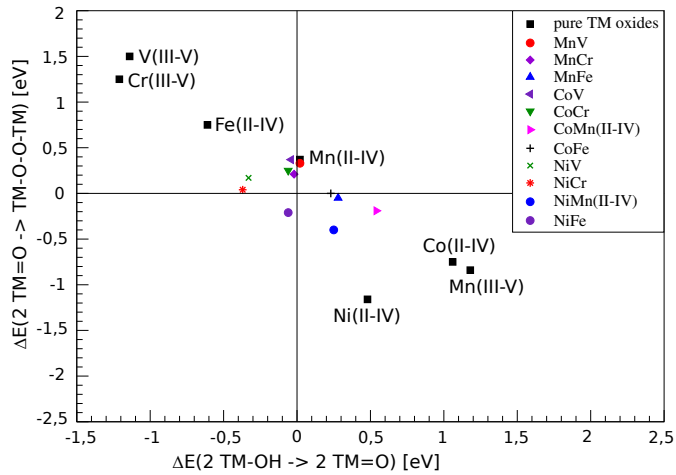

Figure 16: A comparison between the catalytic performance of the homonuclear 3d TM oxides and the heteronuclear catalysts constructed by mixing [+/-] with [-/+] catalysts is shown. The energetics of the heteronuclear catalysts are estimated with the Formulas 33 and 34.

Co(II-IV)Cr(III-V) system. In case of Mn(III-V)Cr(II-IV), Mn(III-V)Fe(II-IV) and Ni(II-IV)V(III-V) the deviations are found to be negliable.

Despite the close agreement between interpolated and calculated values some scatter can still be found. These differences can be attributed to two major sources of errors, the GGA inherent SIE and differential coulombic effects when considering mixed oxidation state systems. The effect of the former is discussed with respect to the V(III-V)Ni(II-IV) and Fe(II-IV)Ni(II-IV) heteronuclear systems for the oxidation of the di-hydroxo to the di-oxo intermediate. The corresponding d-occupation for the involved elements is found to be d^1-d^0 for V(IV-V), d^5-d^4 for Fe(III-IV) and d^7-d^6 for Ni(III-IV). While vanadium and iron can be considered unproblematic due to the missing ambiguity in spin state for the former and the pure high spin configuration for iron, nickel may be expected to be problematic since both high and low spin configurations are possible. Starting the discussion with the Ni(III)Fe(III) di-hydroxo species, the low spin septet state is found to be 0.4 eV more stable compared to the nonet high spin state. In case of the Ni(IV)Fe(IV) di-oxo intermediate the high spin state is stabilized by 0.2 eV. Similar results are obtained in case of the V(III-V)Ni(II-IV) system. Here,

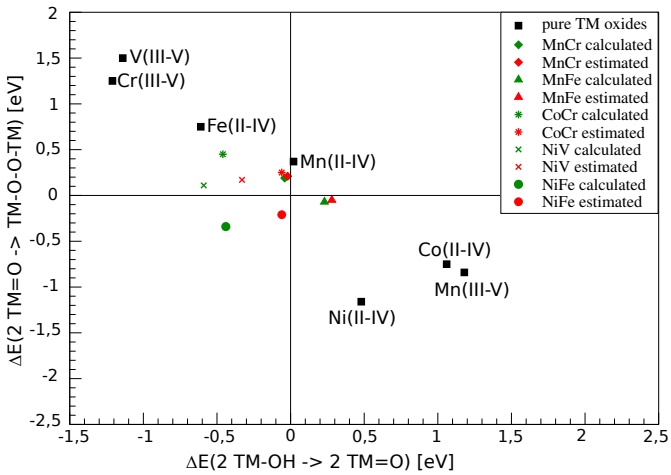

Figure 17: The direct comparison between the calculated and estimated energy profile for selected mixed TM systems is depicted.

the low spin triplet state is more stable by 0.2 eV for the di-hydroxo intermediate while the high spin nonet state is the ground state in case of the di-oxo intermediate. The effects are however comparably small. Thus, it is unlikely that the results discussed above will be changed by this ambiguity in the description of the relative stabilities of spin states.

A second source of errors are the differential coulombic effects resulting from the differences in Madelung potential between the TM(II-IV) and TM(III-V) systems. While this difference is not included in the simple approximation used to predict the reactivity of the heteronuclear systems it is treated explicitly in the DFT calculations used to evaluate the validity of the procedure. In case of a TM(III)TM(IV) system the exact Coulomb repulsion as included in the DFT calculations is $12e^2/R$, compared to $12.5e^2/R$ when employing the homonuclear systems to approximate them. Similarly a slightly higher Coulomb repulsion is found for the TM(IV)TM(V) system (exact: $20e^2/R$; estimated: $20.5e^2/R$). The numbers come again out small. Thus, no changes in the qualitative results discussed above are expected.

Summing up, mixing transition metal oxides of the [+/-] and [-/+] class is a viable possibility to increase the catalytic performance of water oxidation cat-

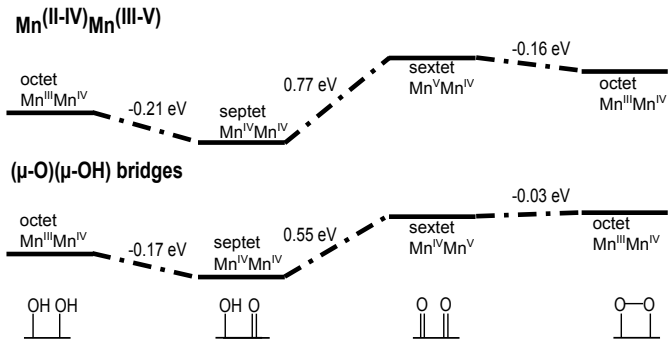

Figure 18: The energy profile of mixed Mn(II-IV)Mn(III-V) dimers embedded into a $MgO_x(OH)_y$ rig for the di-hydroxo - oxo-hydroxo - di-oxo - μ-peroxo path is displayed.

alysts. Such an improvement compared to the pure TM oxides is indeed also found experimentally[23, 136, 141–144].

4.3.4 Mixed Oxidation State Catalysts

In Figure 12 the results for the OER assuming a Mn(II-IV) and Mn(III-V) system were summarized and Mn(II-IV) was discussed with respect to Ir(III-V) in Section 4.3.1. One key finding of this section was that the Mn(II-IV) system is, despite its promising energetics not able to oxidize water and evolve O_2 due to kinetic hindrance. Mn(III-V) on the other hand can sustain the water oxidation reaction at the price of a high overpotential. It was recently found in experiment that the overpotential of a manganese oxide catalyst is lowered by dissolution of manganese[145]. When assuming the dissolution to result in an increase of defects this finding may be understood in terms of the mixed transition metal oxide catalysts discussed in Section 4.3.3.

Similar to these mixed TM oxides Mn(II-IV) may be mixed with Mn(III-V). In contrast to mixed transition metal oxide systems such mixed oxidation state systems may be obtained in several ways. In the present work two possibilities are considered. One possibility comprises the removal of a hydrogen from the bridging OH groups and the second possibility considered, the removal of a hydrogen from the trans standing H_2O equivalent unit. The energy profile for

an assumed binuclear mechanism is shown in Figure 18. Similar to the mixed TM systems, the energy profile of the distinct Mn(II-IV) Mn(III-V) system is found to reflect the energetics of the pure oxides. Assuming the oxidation steps to proceed via the oxidation of the Mn(III)-OH moiety to Mn(IV)=O in the first step followed by the formation of Mn(V)=O, the former step is found exothermic by 0.21 eV, compared to an exothermicity of 0.33 eV for the pure Mn(II-IV) dimer site. The subsequent oxidation to from Mn(V)=O is then found endothermic by 0.77 eV compared to 0.66 eV for the pure system. Due to the endothermicity of the Mn(IV-V) couple, the resulting O-O bond formation energy is exothermic by 0.16 eV. Thus, the exothermicity of this step is reduced to its bare minimum.

The second situation where mixed oxidation state systems might be formed is by deprotonation of a bridging μ-OH moiety resulting in the formation of a μ-O bridge. The energy profile of such a situation is shown in Figure 18. The oxidation steps are found to be exothermic by 0.17 eV followed by an Mn(V)=O formation endothermic by 0.55 eV which results in a approximately thermoneutral O-O bond formation. The differences between the distinct Mn(II-IV) Mn(III-V) and the present system may be attributed to a buffering effect of the μ-O μ-OH bridge.

A second effect of the mixing of an unreactive Mn(IV)=O with a reactive Mn(V)=O is the expected reduction in the activation barrier. This can be understood considering the fact that in contrast to the Mn(II-IV) dimer only one expensive Mn(IV)=O bond needs to be broken. Thus, both from a kinetic and a thermodynamic point of view the overall performance of these mixed Mn(II-IV) Mn(III-V) systems is improved and may explain the experimentally found enhancement in reactivity.

5 CONCLUSIONS AND OUTLOOK

CONCLUSIONS

- The central reaction steps of a binuclear OER mechanism are the oxidation of TM-OH to form TM=O and the subsequent μ-peroxo O-O bond formation. The energy profile of these steps depends on the relative stability of the TM=O intermediate. For example, in case of a Mn(III-V) molecular model system an endothermic oxidation step followed by an exothermic O-O bond formation combined with a low activation barrier is found.
- The use of the energetics for oxidation of TM-OH to form TM=O and subsequent O-O bond formation as descriptor was validated for a series of 3d TM oxide candidate catalysts embedded into a $MgO_x(OH)_y$ test rig.
- At the TyrOH/TyrO$^\bullet$ reference potential two classes of catalysts emerge:
- Class 1 contains Mn(III-V), Co(II-IV) and Ni(II-IV). It shows an endothermic oxidation step followed by exothermic μ-peroxo bond formation ([+/-] class). These catalysts are active towards the OER at the price of a comparably high overpotential.
- Class 2 exhibits opposite behavior, e.g. an exothermic oxidation step followed by endothermic O-O bond formation. V(III-V), Cr(III-V) and Fe(II-IV) belong to this class. Due to the endothermicity of the O-O bond formation these oxides are argued to be inactive towards the OER.
- Intermediate behavior is found for mixed TM oxides, which combine one TM from each group. These catalysts facilitate the oxidation of a TM-OH moiety to form TM=O at the TyrOH/TyrO$^\bullet$ reference potential. Correspondingly, the subsequent O-O bond formation is approximately thermoneutral. Thus, superior performance compared to the pure 3d TM oxides can be expected. This finding is in agreement with experiment[23, 136, 141–144].

- Similar to the mixed TM oxides Mn(II-IV) and Ir(III-V) show near ideal behavior. While the latter is active towards oxygen evolution the former is argued to be inactive due to a high activation barrier for O-O bond formation.
- An improvement of the activity of manganese as an OER catalyst is achieved in mixed Mn(II-IV) Mn(III-V) systems. Such a mixed oxidation state situation might be found at defects.

OUTLOOK

- Ligand and embedding effects were only touched upon in the present work. These effects may influence the performance of an OER catalyst. Particularly in the case of molecular OER catalysts significant dependence of the performance on choice of ligands is expected. A combined theoretical and experimental study of these effects would offer an interesting target, which promises to be fruitful.
- The results presented here have direct implications for understanding the OER in PS II. The catalytic performance of this system may indeed be understood in terms of an embedded binuclear site comprising a mixed oxidation state system.
- Utilization of the methodology in general and in particular of the binuclear mechanism to several other reactions might prove valuable. Electrocatalytic reactions of interest would include oxidation of ammonia, reduction of NO_x, reduction of ClO_3^- as well as N_2 fixation.

6 ACKNOWLEDGMENTS

Over the last years I had the possibility to meet many interesting people who helped with big and small things. Without them a lot of things would not have been possible:

Itai Pans: Thank you for supervising me, the freedom you gave me in my research and for teaching me so much about quantum chemistry and DFT. I would also like thank you for always having an open door. I enjoyed the many long, enthusiastic, interesting, inspiring and helpful discussion ranging from water oxidation to quantum chemistry and from superconductivity to politics.

Elisabet Ahlberg: Thank you for believing in me and giving me the chance to pursue my doctoral studies in your group. I am also grateful that you helped me broadening my horizon by teaching me electrochemistry and confronting me with the experimentalist's perspective.

It was great to work with both of you!

Thanks also to all my former and present colleagues *Adriano, Anders, Andrea, Jakub, Johanna, Kristoffer, Gert, Patrick and Zareen* for the good time and helping me understand the experimentalist's perspective.

I would especially like to thank my room mate *Patrick* for supplying me with Figure 13. And good luck with your defense on June 4th.

Angelica, finally I would also like to thank you for giving me that little hint that brought me to Gothenburg. I guess with out you I would not have started this fascinating project...

Furthermore I would like thank all the ELCAT fellows I had the chance to meet over the last years for the great time and the many interesting discussions during the ELCAT meetings.

Thanks also to *Martin* for helping with some LaTeX problems and proof reading.

Zum Schluß möchte ich auch meinen Eltern danken daß sie mir überhaupt das Studium ermöglicht haben und mich während der letzten Jahre uneingeschränkt unterstützt haben. In diesem Sinne ist es glaube ich höchste Zeit einfach einmal "Danke" zu sagen.

The present work was performed within the framework of the "ELCAT" initial training network and financed by the European Union (Grant Agreement No. 214936-2).

BIBLIOGRAPHY

[1] M. Midilli, A. Ay, I. Dincer, M. A. Rosen, *Renew. Sust. Energ. Rev.* **2005**, *9*, 256–271.

[2] R. Schlögl, *Angew. Chem. Int. Ed.* **2011**, *50*, 6424–6426; *Angew. Chem.* **2011**, *123*, 6550–6553.

[3] H. Dau, C. Limberg, T. Reier, M. Risch, S. Roggan, P. Strasser, *ChemCatChem.* **2010**, *2*, 724–761.

[4] H. Gerischer, *Bull. Soc. Chim. Belg.* **1958**, *67*, 506–527.

[5] S. Trasatti, *J. Electroanal. Chem.* **1972**, *39*, 163–184.

[6] J. Greeley, T. F. Jaramillo, J. Bonde, I. Chorkendorff, J. K. Nørskov, *Nature Materials* **2006**, *5*, 909–913.

[7] D. V. Esposito, S. T. Hunt, A. L. Stottlemyer, K. D. Dobson, B. E. McCandless, R. W. Birkmire, J. G. Chen, *Angew. Chem. Int. Ed.* **2010**, *49*, 9859–9862; *Angew. Chem.* **2010**, *122*, 10055–10058.

[8] V. Artero, M. Fontecave, M. Chavarot-Kerlidou, *Angew. Chem. Int. Ed.* **2011**, *50*, 7238–7266; *Angew. Chem.* **2011**, *123*, 7376–7405.

[9] A. Le Goff, V. Artero, B. Jousselme, P. Tran, N. Guillet, R. Métayé, A. Fihri, S. Palacin, M. Fontecave, *Science* **2009**, *326*, 1384–1387.

[10] G. Lodi, E. Sivieri, A. De Battisti, S. Trasatti, *J. Appl. Electrochem.* **1978**, *8*, 135–143.

[11] J. O. Bockris, T. Otagawa, *J. Phys. Chem.* **1983**, *87*, 2960–2971.

[12] *H. Beer*, *US patent* 710551, **1958**.

[13] *H. Beer*, *US patent* 3711385, **1971**.

[14] S. Trasatti, *Electrochim. Acta* **2000**, *45*, 2377–2385.

[15] C. Comninellis, G. P. Vercesi, *J. Appl. Electrochem.* **1991**, *21*, 335–345.

[16] M. Morita, C. Iwakura, H. Tamura, *Electrochim. Acta* **1978**, *23*, 331–335.

[17] L. Nylén, A. Cornell, *J. Electrochem. Soc.* **2006**, *153*, D14–D20.

[18] M. S. El-Deab, M. I. Awad, A. M. Mohammad, T. Ohsaka, *Electrochem. Commun.* **2007**, *9*, 2082–2087.

[19] A. M. Mohammad, M. I. Awad, M. S. El-Deab, T. Okajima, T. Ohsaka, *Electrochim. Acta* **2008**, *53*, 4351–4358.

[20] M. W. Kanan, D. G. Nocera, *Science* **2008**, *321*, 1072–1075.

[21] N. H. Chou, P. N. Ross, A. T. Bell, T. D. Tilley, *ChemSusChem* **2011**, *4*, 1566–1569.

[22] F. Jiao, H. Frei, *Angew. Chem. Int. Ed.* **2009**, *48*, 1841–1844; *Angew. Chem.* **2009**, *121*, 1873–1876.

[23] M. Hamdani, R. N. Singh, P. Chartier, *Int. J. Electrochem. Sci* **2010**, *5*, 556–577.

[24] K. N. Ferreira, T. M. Iverson, K. Maghlaoui, J. Barber, S. Iwata, *Science* **2004**, *303*, 1831–1838.

[25] Y. Umena, K. Kawakami, J. Shen, N. Kamiya, *Nature* **2011**, *473*, 55–61.

[26] B. Loll, J. Kern, W. Saenger, A. Zouni, J. Biesiadka, *Nature* **2005**, *438*, 1040–1044.

[27] A. Grundmeier, H. Dau, *Biochim. Biophys. Acta* **2012**, *1817*, 88–105.

[28] E. M. Sproviero, J. A. Gascn, J. P. McEvoy, G. W. Brudvig, V. S. Batista, *J. Am. Chem. Soc.* **2008**, *130*, 3428–3442.

[29] J. Rossmeisl, K. Dimitrievski, P. Siegbahn, J. K. Nørskov, *J. Phys. Chem. C* **2007**, *111*, 18821–18823.

[30] G. Renger, *J. Photochem. Photobiol., A* **2011**, *104*, 35–43.

[31] B. Andersson, A. H. Salter, I. Virgin, I. Vass, S. Styring, *J. Photochem. Photobiol., B* **1992**, *15*, 15–31.

[32] M. Hakala, I. Tuominen, M. Keränen, T. Tyystjärvi, E. Tyystjärvi, *Biochim. Biophys. Acta* **2005**, *1706*, 68–80.

[33] D. Gust, T. A. Moore, A. L. Moore, *Faraday Discuss.* **2012**, *155*, 9–26.

[34] W. Rüttinger, G. C. Dismukes, *Chem. Rev.* **1997**, *97*, 1–24.

[35] M. Yagi, M. Kaneko, *Chem. Rev.* **2001**, *101*, 21–36.

[36] X. Liu, *Coord. Chem. Rev.* **2012**, *256*, 1115–1136.

[37] J. K. Hurst, *Coord. Chem. Rev.* **2005**, *249*, 313–328.

[38] S. W. Gersten, G. J. Samuels, T. J. Meyer, *J. Am. Chem. Soc.* **1982**, *104*, 4029–4030.

[39] R. A. Binstead, C. W. Chronister, J. Ni, C. M. Hartshorn, , T. J. Meyer, *J. Am. Chem. Soc.* **2000**, *122*, 8464–8473.

[40] J. J. Concepcion, M. Tsai, J. T. Muckerman, T. J. Meyer, *J. Am. Chem. Soc.* **2010**, *132*, 1545–1557.

[41] J. Limburg, G. W. Brudvig, R. H. Crabtree, *J. Am. Chem. Soc.* **1997**, *119*, 2761–2762.

[42] J. Limburg, J. S. Vrettos, H. Chen, J. C. de Paula, R. H. Crabtree, G. W. Brudvig, *J. Am. Chem. Soc* **2001**, *123*, 423–430.

[43] M. Lundberg, M. R. A. Blomberg, P. E. M. Siegbahn, *Inorg. Chem* **2004**, *43*, 264–274.

[44] A. K. Poulsen, A. Rompel, C. J. McKenzie, *Angew. Chem. Int. Ed.* **2005**, *44*, 6916–6920; *Angew. Chem.* **2005**, *117*, 7076–7080.

[45] J. Blakemore, N. Schley, D. Balcells, J. Hull, G. Olack, C. Incarvito, O. Eisenstein, G. Brudvig, R. Crabtree, *J. Am. Chem. Soc.* **2010**, *132*, 16017–16029.

[46] J. F. Hull, D. Balcells, J. D. Blakemore, C. D. Incarvito, O. Eisenstein, G. W. Brudvig, R. H. Crabtree, *J. Am. Chem. Soc.* **2009**, *131*, 8730–8731.

[47] J. Rossmeisl, A. Logadottir, J. K. Nørskov, *Chem. Phys.* **2005**, *319*, 178–184.

[48] J. Rossmeisl, Z. Qu, H. Zhu, G. Kroes, J. K. Nørskov, *J. Electroanal. Chem.* **2007**, *607*, 83–99.

[49] R. Parsons, *Trans. Faraday Soc.* **1958**, *54*, 1053–1063.

[50] J. K. Nørskov, , J. Rossmeisl, A. Logadottir, L. Lindqvist, J. R. Kitchin, T. Bligaard, H. Jónsson, *J. Phys. Chem. B* **2004**, *108*, 17886–17892.

[51] E. Schrödinger, *Ann. Phys.* **1926**, *384*, 361–376.

[52] M. Born, *Z. Phys.* **1926**, *37*, 863–867.

[53] J. J. Sakurai, *Modern Quantum Mechanics 1st ed.*, Addison Wesley, Reading, Massachusetts, **1994**.

[54] F. Schwabl, *Quantenmechanik (QM1) 6th ed.*, Springer, Berlin, **2005**.

[55] M. Born, R. Oppenheimer, *Ann. Phys.* **1927**, *389*, 457–484.

[56] A. Szabo, N. S. Ostlund, *Modern Quantum Chemistry - Introduction to Advanced Electronic Structure Theory*, Mc Graw-Hill Publishing Company, New York, **1982**.

[57] A. Groß, *Theoretical Surface Science - A Microscopic Perspective*, Springer-Verlag, Berlin, Heidelberg, **2003**.

[58] D. R. Hartree, *Proc. Camb. Phil. Soc.* **1928**, *24*, 89–110.

[59] D. R. Hartree, *Proc. Camb. Phil. Soc.* **1928**, *24*, 111–132.

[60] V. Fock, *Z. Phys.* **1930**, *61*, 126–148.

[61] V. Fock, *Z. Phys.* **1930**, *62*, 795–805.

[62] J. C. Slater, *Phys. Rev.* **1930**, *35*, 210–211.

[63] J. A. Pople, *Rev. Mod. Phys.* **1999**, *71*, 1267–1274.

[64] C. J. Cramer, D. G. Truhlar, *Phys. Chem. Chem. Phys.* **2009**, *11*, 10757–10816.

[65] P. Hohenberg, W. Kohn, *Phys. Rev. B* **1964**, *136*, B864–B871.

[66] W. Kohn, *Rev. Mod. Phys.* **1999**, *71*, 1253–1266.

[67] W. Koch, M. C. Holthausen, *A Chemist's Guide to Density Functional Theory 2nd ed.*, Wiley-VCH, Weinheim, **2001**.

[68] W. Kohn, L. J. Sham, *Phys. Rev. A* **1965**, *140*, A1133–A1138.

[69] D. Cremer, *Mol. Phys.* **2001**, *99*, 1899–1940.

[70] V. Polo, E. Kraka, D. Cremer, *Mol. Phys.* **2002**, *100*, 1771–1790.

[71] D. M. Ceperley, B. J. Alder, *Phys. Rev. Lett.* **1980**, *45*, 566–569.

[72] W. Kohn, A. D. Becke, R. G. Parr, *J. Phys. Chem.* **1996**, *100*, 12974–12980.

[73] A. D. Becke, *Phys. Rev. A* **1988**, *38*, 3098–3100.

[74] J. P. Perdew, W. Yue, *Phys. Rev. B* **1986**, *33*, 8800–8802.

[75] J. P. Perdew, K. Burke, M. Ernzerhof, *Phys. Rev. Lett.* **1996**, *77*, 3865–3868.

[76] C. Lee, W. Yang, R. G. Parr, *Phys. Rev. B* **1988**, *37*, 785–789.

[77] N. C. Handy, *Theor. Chem. Acc.* **2009**, *123*, 165–169.

[78] R. Colle, O. Salvetti, *Theor. Chim. Acta* **1975**, *37*, 329–334.

[79] P. J. Stephens, F. J. Devlin, C. F. Chabalowski, M. J. Frisch, *J. Chem. Phys.* **1994**, *98*, 11623–11627.

[80] M. Reiher, O. Salomon, A. Hess, *Theor. Chem. Acc.* **2001**, *107*, 48–55.

[81] M. Lundberg, P. E. M. Siegbahn, *J. Comput. Chem.* **2005**, *26*, 661–667.

[82] P. E. M. Siegbahn, *J. Biol. Inorg. Chem.* **2006**, *11*, 695–701.

[83] J. P. Perdew, A. Zunger, *Phys. Rev. B* **1981**, *12*, 5048–5079.

[84] A. J. Cohen, P. Mori-Sanchez, W. Yang, *Science* **2008**, *321*, 792–794.

[85] P. Mori-Sanchéz, A. J. Cohen, W. Yang, *J. Chem. Phys.* **2006**, *125*, 201102.

[86] A. B. Shick, A. I. Liechtenstein, W. E. Pickett, *Phys. Rev. B* **1999**, *60*, 10763–10769.

[87] L. Noodleman, *J. Chem. Phys.* **1981**, *74*, 5737–5743.

[88] L. Noodleman, E. R. Davidson, *Chem. Phys.* **1986**, *109*, 131–143.

[89] P. Mori-Sanchéz, A. J. Cohen, w. Yang, *Phys. Rev. Lett.* **2008**, *100*, 146401.

[90] H. Xiao, J. Tahir-Kheli, W. A. Goddard, III, *Phys. Chem. Lett.* **2011**, *2*, 212–217.

[91] V. I. Anisimov, J. Zaanen, O. K. Andersen, *Phys.Rev. B* **1991**, *44*, 943–954.

[92] S. F. Boys, *Proc. R. Soc. London* **1950**, *200*, 542–554.

[93] E. R. Davidson, D. Feller, *Chem. Rev.* **1988**, *86*, 681–696.

[94] M. Kelterer, A.-M. Ramek, R. F. Frey, M. Cao, L. Schäfer, *J. Mol. Struct.* **1994**, *310*, 45–53.

[95] R. H. Hertwig, W. Koch, *J. Comput. Chem.* **1995**, *16*, 576–585.

[96] B. Delley, *J. Chem. Phys.* **1990**, *92*, 508–517.

[97] P. Schwerdtfeger, *ChemPhysChem* **2011**, *12*, 3143–3155.

[98] D. Vanderbilt, *Phys. Rev. B* **1990**, *41*, 7892–7895.

[99] G. Henkelmann, H. Jónsson, *J. Chem. Phys.* **2000**, *113*, 9978–9985.

[100] D. Sheppard, R. Terrell, G. Henkelman, *J. Chem. Phys.* **2008**, *128*, 134106.

[101] T. Halgren, W. Lipscomb, *Chem. Phys. Lett.* **1977**, *49*, 225–232.

[102] N. Govind, M. Petersen, G. Fitzgerald, D. King-Smith, J. Andzelm, *Comp. Mater. Sci* **2003**, *28*, 250–258.

[103] A. Lundin, I. Panas, E. Ahlberg, *J. Phys. Chem. A* **2007**, *111*, 9080–9086.

[104] M. Frisch, G. Trucks, H. Schlegel, G. Scuseria, M. Robb, J. Cheeseman, J. Montgomery Jr., T. Vreven, K. Kudin, J. Burant, J. Millam, S. Iyengar, J. Tomasi, V. Barone, B. Mennucci, M. Cossi, G. Scalmani, N. Rega, G. Petersson, H. Nakatsuji, M. Hada, M. Ehara, K. Toyota, R. Fukuda, J. Hasegawa, M. Ishida, T. Nakajima, Y. Honda, O. Kitao, H. Nakai, M. Klene, X. Li, J. Knox, H. Hratchian, J. Cross, V. Bakken, C. Adamo, J. Jaramillo, R. Gomperts, R. Stratmann, O. Yazyev, A. Austin,

R. Cammi, C. Pomelli, J. Ochterski, P. Ayala, K. Morokuma, G. Voth, P. Salvador, J. Dannenberg, V. Zakrzewski, S. Dapprich, A. Daniels, M. Strain, O. Farkas, D. Malick, A. Rabuck, K. Raghavachari, J. Foresman, J. Ortiz, Q. Cui, A. Baboul, S. Clifford, J. Cioslowski, B. Stefanov, G. Liu, A. Liashenko, P. Piskorz, I. Komaromi, R. Martin, D. J. Fox, T. Keith, M. Al-Laham, C. Peng, A. Nanayakkara, M. Challacombe, P. Gill, B. Johnson, W. Chen, M. Wong, C. Gonzalez, J. Pople, *Gaussian 03, Revision E.01*, Gaussian, Inc., Wallingford CT, **2004**.

[105] R. Pulay, *Chem. Phys. Lett.* **1980**, *73*, 393–398.

[106] P. Pulay, *J. Comput. Chem.* **1982**, *3*, 556–560.

[107] S. J. Clark, M. D. Segall, C. J. Pickard, P. J. Hasnip, M. J. Probert, K. Refson, M. C. Payne, *Z. Kristallogr.* **2005**, *220*, 567–570.

[108] *Materials Studio Release 5.0*, **2009**.

[109] B. Delley, *J. Chem. Phys.* **2000**, *113*, 7756–7764.

[110] B. Delley, *Phys. Rev. B* **2002**, *66*, 155125.

[111] J. R. T. Johnsson Wass, I. Panas, J. Åsbjörnsson, E. Ahlberg, *J. Electroanal. Chem.* **2007**, *599*, 295–312.

[112] G. C. Dismukes, J. E. Sheats, J. A. Smegal, *J. Am. Chem. Soc.* **1987**, *109*, 7202–7203.

[113] S. Mukhopadhyay, W. H. Armstrong, *J. Am. Chem. Soc.* **2003**, *125*, 13010–13011.

[114] M. Mitani, Y. Wakamatsu, T. Katsurada, Y. Yoshioka, *J. Phys. Chem. A* **2006**, *110*, 13895–13914.

[115] X. G. Zhao, W. H. Richardson, J. Chen, J. Li, L. Noodleman, H. Tsai, D. N. Hendrickson, *Inorg. Chem.* **1997**, *36*, 1198–1217.

[116] K. P. Jensen, B. O. Roos, U. Ryde, *J. Inorg. Biochem.* **2005**, *99*, 45–54.

[117] J. S. Sears, C. D. Sherrill, *J. Chem. Phys.* **2006**, *124*, 144314.

[118] T. Soda, Y. Kitagawa, T. Onishi, Y. Takano, Y. Shigeta, H. Nagao, Y. Yoshioka, K. Yamaguchi, *Chem. Phys. Lett.* **2000**, *319*, 223–230.

[119] K. Yamaguchi, Y. Takahara, T. Fueno, *Applied Quantum Chemistry*, V. H. Smith (Ed.), Reidel, Dodrecht, **1986**.

[120] R. W. Grant, S. Geller, J. A. Cape, G. P. Espinosa, *Phys. Rev.* **1968**, *175*, 686–695.

[121] A. F. Hollemannn, N. Wiberg, *Anorganische Chemie 102nd ed.*, Walter de Gruyter, Berlin, **2007**.

[122] Á. Valdés, Z. Qu, J. Kroes, G.-J. Rossmeisl, J. K. Nørskov, *J. Phys. Chem. C* **2008**, *112*, 9872–9879.

[123] I. C. Man, H. Su, F. Calle-Vallejo, H. A. Hansen, N. G. Martìnez, J. I. Inoglu, J. Kitchin, T. F. Jaramillo, J. K. Nørskov, J. Rossmeisl, *ChemCatChem.* **2011**, *3*, 1159–1165.

[124] P. E. M. Siegbahn, M. R. A. Blomberg, *Biochim. Biophys. Acta* **2004**, *1655*, 45–50.

[125] G. Rengner, *Photosynth. Res.* **2007**, *92*, 407–425.

[126] A. Harriman, *J. Phys. Chem.* **1987**, *91*, 6102–6104.

[127] S. V. Jovanovic, A. Harriman, M. G. Simic, *J. Phys. Chem.* **1986**, *90*, 1935–1939.

[128] D. R. Lide (Ed.), *CRC Handbook of Chemistry and Physics 85th ed.*, CRC Press, Boca Raton, **2004**.

[129] L. Wang, Q. Wu, T. Van Voorhis, *Inorg. Chem.* **2010**, *49*, 4543–4553.

[130] X. Yang, M. Baik, *J. Am. Chem. Soc.* **2008**, *130*, 16231–16240.

[131] J. E. McGrady, R. Stranger, *Inorg. Chem.* **1999**, *38*, 550–558.

[132] U. Bossek, T. Weyhermueller, K. Wieghardt, B. Nuber, J. Weiss, *J. Am. Chem. Soc.* **1990**, *112*, 6387–6388.

[133] P. E. M. Siegbahn, *Chem. Eur. J.* **2008**, *14*, 8290–8302.

[134] L. Grajciar, O. Bludský, P. Nachtigall, *J. Phys. Chem. Lett.* **2010**, *1*, 3354–3359.

[135] A. J. Esswein, M. J. McMurdo, P. N. Ross, A. T. Bell, T. D. Tilley, *J. Phys. Chem. C* **2009**, *113*, 15068–15072.

[136] R. N. Singh, N. K. Singh, J. P. Singh, *Electrochim. Acta* **2002**, *47*, 3873–3879.

[137] A. Marshall, B. Børresen, G. Hagen, M. Tsypkin, R. Tunold, *Electrochim. Acta* **2006**, *51*, 3161–3167.

[138] E. Slavcheva, I. Radev, S. Bliznakov, G. Topalov, P. Andreev, E. Budevski, *Electrochim. Acta* **2007**, *52*, 3889–3894.

[139] A. R. Hillman, M. A. Skopek, S. J. Gurman, *Phys. Chem. Chem. Phys.* **2011**, *13*, 5252–5263.

[140] P. E. M. Siegbahn, R. H. Crabtree, *J. Am. Chem. Soc* **1999**, *121*, 117–127.

[141] N. K. Singh, S. K. Tiwari, K. L. Anitha, R. N. Singh, *Faraday Trans.* **1996**, *92*, 2397–2400.

[142] E. Rios, P. Chartier, J. L. Gautier, *Solid State Sci.* **1999**, *1*, 267–277.

[143] M. D. Merrill, R. C. Dougherty, *J. Phys. Chem. C* **2008**, *112*, 3655–3666.

[144] M. D. Merrill, Ph.D. thesis, The Florida State University - College of Arts and Sciences, **2007**.

[145] Y. Chu, C. Hu, K. Chang, *Electrochim. Acta* **2012**, *61*, 124–131.